

Three-dimensional pure deflagration models with nucleosynthesis and synthetic observables for Type Ia supernovae

Michael Fink,^{1★} Markus Kromer,^{2,3} Ivo R. Seitenzahl,^{1,2}
Franco Ciaraldi-Schoolmann,² Friedrich K. Röpkke,¹ Stuart A. Sim,⁴
Rüdiger Pakmor,⁵ Ashley J. Ruiter² and Wolfgang Hillebrandt²

¹*Institut für Theoretische Physik und Astrophysik, Universität Würzburg, Emil-Fischer-Straße 31, D-97074 Würzburg, Germany*

²*Max-Planck-Institut für Astrophysik, Karl-Schwarzschild-Straße 1, D-85748 Garching, Germany*

³*The Oskar Klein Centre, Stockholm University, AlbaNova, SE-106 91 Stockholm, Sweden*

⁴*Astrophysics Research Centre, School of Mathematics and Physics, Queen's University Belfast, Belfast BT7 1NN, UK*

⁵*Heidelberger Institut für Theoretische Studien, Schloss-Wolfsbrunnengasse 35, D-69118 Heidelberg, Germany*

Accepted 2013 November 29. Received 2013 November 29; in original form 2013 August 14

ABSTRACT

We investigate whether pure deflagration models of Chandrasekhar-mass carbon–oxygen white dwarf stars can account for one or more subclass of the observed population of Type Ia supernova (SN Ia) explosions. We compute a set of 3D full-star hydrodynamic explosion models, in which the deflagration strength is parametrized using the multispot ignition approach. For each model, we calculate detailed nucleosynthesis yields in a post-processing step with a 384 nuclide nuclear network. We also compute synthetic observables with our 3D Monte Carlo radiative transfer code for comparison with observations. For weak and intermediate deflagration strengths (energy release $E_{\text{nuc}} \lesssim 1.1 \times 10^{51}$ erg), we find that the explosion leaves behind a bound remnant enriched with 3 to 10 per cent (by mass) of deflagration ashes. However, we do not obtain the large kick velocities recently reported in the literature. We find that weak deflagrations with $E_{\text{nuc}} \sim 0.5 \times 10^{51}$ erg fit well both the light curves and spectra of 2002cx-like SNe Ia, and models with even lower explosion energies could explain some of the fainter members of this subclass. By comparing our synthetic observables with the properties of SNe Ia, we can exclude the brightest, most vigorously ignited models as candidates for any observed class of SN Ia: their $B - V$ colours deviate significantly from both normal and 2002cx-like SNe Ia and they are too bright to be candidates for other subclasses.

Key words: hydrodynamics – nuclear reactions, nucleosynthesis, abundances – radiative transfer – supernovae: general – white dwarfs.

1 INTRODUCTION

It is generally accepted that Type Ia supernovae (SNe Ia) originate from a thermonuclear explosion of a carbon–oxygen white dwarf (CO WD) in an interacting binary system (see Wang & Han 2012, for a current review on constraints on the progenitor system). However, despite decades of research, SNe Ia remain incompletely understood: neither the exact nature of their progenitor systems nor the burning mode in which the explosions proceed are clearly identified.

A well-established progenitor channel is the single-degenerate Chandrasekhar-mass (M_{Ch}) scenario, in which the companion star

to the WD is either a main-sequence or evolved non-degenerate star. In this scenario, the explosion is triggered when the WD approaches M_{Ch} due to accretion from its companion. Recent observations of time-varying Na features in the spectra of some SNe Ia point towards a single-degenerate origin (Patat et al. 2007; Sternberg et al. 2011; Dilday et al. 2012); the Na features may be interpreted as signatures of nova shells that were expelled from the WD during the accretion phase (see, however, Shen, Guillochon & Foley 2013; Soker et al. 2013 for alternative explanations).

Within the single-degenerate scenario, several explosion mechanisms are possible (see Hillebrandt & Niemeyer 2000 for a review). It is known that the explosion has to start as a subsonic deflagration. Unlike for a prompt detonation, a deflagration allows parts of the WD to expand significantly before being burnt. Thus, a sufficient amount of intermediate-mass elements (IMEs), such as Si,

* E-mail: mfink@astro.uni-wuerzburg.de

can be produced, as needed to explain observed SN Ia spectra. To be consistent with normal SNe Ia, the explosion likely has to turn into a detonation at later burning stages (so-called delayed detonation models) to reproduce the abundance stratification inferred from spectral evolution (e.g. Stehle et al. 2005) and also to reach observed brightnesses/explosion energies. There are different mechanisms that could trigger such a secondary detonation. In the deflagration-to-detonation transition scenario (DDT; Blinnikov & Khokhlov 1986, 1987; Khokhlov 1991), the deflagration is supposed to spontaneously turn into a detonation at late burning stages after the flame has entered the distributed burning regime. Other scenarios initiate a detonation in regions that are compressed due to fallback of hot deflagration ashes that stay gravitationally bound [e.g. so-called gravitationally confined detonation (GCD) scenarios; cf. Plewa, Calder & Lamb 2004; see Section 4.4 for details].

Despite substantial modelling efforts (Ciaraldi-Schoolmann, Seitenzahl & Röpke 2013), DDTs are still not well understood, and Niemeyer (1999) even argue that they may not occur at all. The success of the GCD-like scenarios depends on the amount of energy released in the deflagration and thus on the details of the initial flame geometry, which are not well constrained yet. Therefore, some explosions likely occur as pure deflagrations. This scenario has been suggested as potential explanation of the peculiar subclass of 2002cx-like SNe Ia (Branch et al. 2004; Jha et al. 2006; Phillips et al. 2007).

Apart from the single-degenerate M_{Ch} scenario, there are alternative models for SNe Ia (see e.g. Hillebrandt et al. 2013). Both violent WD–WD mergers (Pakmor et al. 2013; Ruitter et al. 2013) and sub-Chandrasekhar double detonations (Fink et al. 2010; Kromer et al. 2010; Woosley & Kasen 2011; Moll & Woosley 2013) may account for normal and subluminous types of SNe Ia. However, the mixed abundance patterns of 2002cx-like SNe Ia (inferred from their peculiar spectra; Jha et al. 2006; Phillips et al. 2007) seem to be inconsistent with those scenarios, in which explosive burning takes place as detonation (resulting in layered abundance patterns). Thus, M_{Ch} pure deflagrations may still be required in order to explain the full range of subclasses of SNe Ia.

Pure deflagrations have been studied extensively in numerical simulations (cf. Reinecke, Hillebrandt & Niemeyer 2002b; Gamezo et al. 2003; García-Senz & Bravo 2005; Röpke et al. 2006a,b, 2007b; Jordan et al. 2012b; Long et al. 2013; Ma et al. 2013 for recent multidimensional studies). To investigate their potential contribution to the observed sample, we carry out an extensive study of pure deflagrations in 3D Chandrasekhar-mass models for a very wide range of explosion strengths, including detailed nucleosynthetic post-processing and for the first time multidimensional radiative transfer for pure deflagrations (only for one of the models of this study, N5def, synthetic observables have already been published in a companion paper, Kromer et al. 2013). The computed synthetic observables can be directly compared to real observations, which allows us both to constrain the assumed range of initial flame geometries and to investigate which classes of observed SNe Ia might be explained with pure deflagration models.

This study is organized as follows. In Section 2, we present our WD models and the initial flame geometries that are used to initiate deflagration burning in our simulations. Our numerical methods are summarized in Section 3. Then, we present the results of our hydrodynamic simulations (Section 4) and our nucleosynthesis calculations (Section 5). In Section 6, we show the outcomes of our radiative transfer calculations and compare our synthetic light curves and spectra with observations of real supernovae (SNe). Finally, we summarize our results in Section 7.

2 EXPLOSION SCENARIO

In this work, we perform 3D hydrodynamic calculations to simulate the explosion of a full WD star. Our simulations are closely related to those in Seitenzahl et al. (2013, hereafter referred to as S13); we use the same initial WD models and identical setups for the deflagrations. In contrast to S13, however, we assume that no delayed detonation occurs and consider the corresponding pure deflagration models. In the following, we summarize the main parameters of our models (see S13 for further details).

In our standard initial models, we adopt M_{Ch} CO WDs in hydrostatic equilibrium, each with a central density of $\rho_c = 2.9 \times 10^9 \text{ g cm}^{-3}$ and a constant temperature $T = 5 \times 10^5 \text{ K}$. To test the influence of the central density, two models were set up with different central densities of 1.0 and $5.5 \times 10^9 \text{ g cm}^{-3}$ (N100Ldef and N100Hdef). All models assume a homogeneous initial composition with mass fractions $X_{^{12}\text{C}} = 0.475$, $X_{^{16}\text{O}} = 0.50$ and $X_{^{22}\text{Ne}} = 0.025$, which approximately correspond to a solar metallicity of the zero-age main-sequence progenitor star that evolved to the WD.

We start our simulations at the onset of the thermonuclear explosion and do not simulate the previous evolution. As argued in S13, the conditions at the deflagration ignition are not finally settled. Thus, in this study (as in S13) we use the pragmatic approach of igniting the deflagration in multiple spherical ignition spots that start burning simultaneously (so-called multispot ignition) and treat the ignition geometry as a free parameter. In the case of a large number of ignition spots, the flame is effectively always ignited centrally. Such central ignitions with many seeds for instabilities have been found to be the only way of allowing pure deflagration explosions that reach the brightness of (faint) normal SNe Ia (Röpke et al. 2006b; but, see also Ma et al. 2013, who find even larger ^{56}Ni masses). In the case of a small number of ignition spots, the outermost ignition spot tends to dominate the burning, which leads to a one-sided deflagration flame in most of our models. This is consistent with the results of recent pre-ignition simulations that predict bipolar flows through the centre in the simmering phase and a one-sided off-centre ignition (Nonaka et al. 2012). Rotation, on the other hand, could suppress such bipolar flows and render a central ignition more likely.

With our multiple ignition spot parametrization we cannot cover all potential initial flame geometries, but we can access a wide range of explosion strengths in a numerically well-behaved manner (see S13, for details). We assume ignitions in $N_k = 1, 3, 5, 10, 20, 40, 100, 150, 200, 300$ and 1600 (two realizations) sparks placed randomly around the centre of the WD (see Fig. 1).¹ Two models (N300Cdef and N1600Cdef) are constructed to have a very dense arrangement of the ignition kernels (with low r_{max}) and are referred to as ‘compact’ models with an additional ‘C’ in the model name. All other models (with standard initial WD) are depicted ‘standard’ models. The models with alternative central densities (N100Ldef and N100Hdef) use exactly the same spatial positions of the ignition sparks as the N100def model. The radius R_k of the spherical ignition kernels is always 10 km. Only model N300C, which has the most compact configuration with large N_k , uses a lower value of $R_k = 5 \text{ km}$.

¹ We stress that values of N_k as high as 1600 are merely used to parametrize a central deflagration that is already strongly developed at early explosion stages. Physically, deflagration ignition is not likely to occur simultaneously in such a large number of spots.

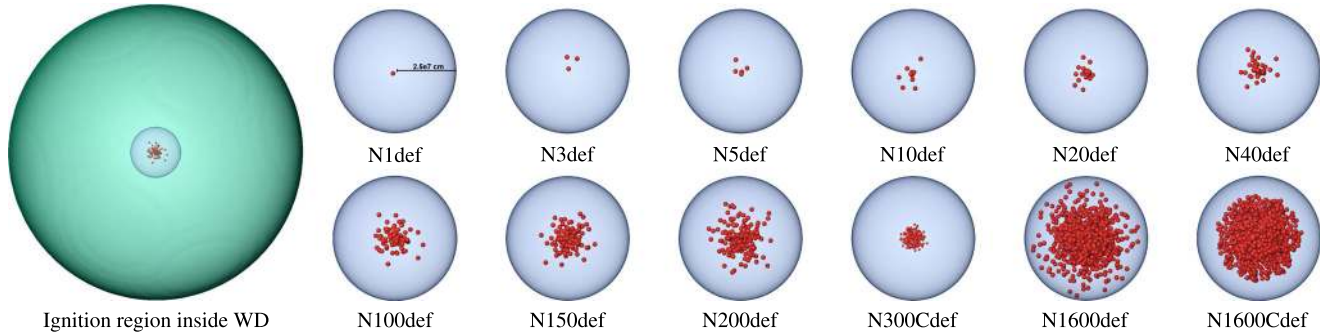


Figure 1. Ignition geometries of our deflagration models. Shown are the ignition kernels (red spheres) and a transparent blue contour where the distance to the centre is 250 km. The maximum radii r_{max} of the ignition kernel distributions are 36, 67, 81, 91, 91, 137, 130, 146, 172, 65, 250 and 180 km, respectively. The leftmost panel shows the position of the ignition regions within the WD.

3 NUMERICAL METHODS

In our simulations, we use the same numerical methods as in S13 and Sim et al. (2013). Therefore, we only give a brief summary here (see above references for more details).

3.1 Hydrodynamic simulation

Our hydrodynamical simulations are carried out in three dimensions with the finite volume hydrodynamics code *LEAFS* (Reinecke, Hillebrandt & Niemeyer 2002a) on a 512^3 -cells ‘hybrid’ moving grid (Röpke 2005). The flame evolution is tracked by an inner Cartesian part of the grid (initial spatial resolution: 1.9 km); the outer parts of the grid, which have exponentially growing cell sizes, track the expansion of the explosion ejecta. With this co-expanding grid, the ejecta evolution is efficiently followed until $t = 100$ s (by which time homologous expansion is a good approximation for most models). This advantage comes at the expense of a poor resolution of the central bound remnants in some of our models (see Section 4.3). We emphasize, however, that our main intention is to derive synthetic observables around peak luminosity. Therefore, we are mainly interested in the ejected material that causes emission at this epoch.

We treat the flame as an infinitesimally thin surface that separates fuel and ashes. The change of position of the flame is described with a level set approach (Osher & Sethian 1988; Smiljanovski, Moser & Klein 1997; Reinecke et al. 1999). Changes of the chemical composition and the release of nuclear energy are performed instantaneously behind the front. We only use a reduced set of five species in the hydrodynamic simulations: ^4He , ^{12}C , ^{16}O , and representative species for both IMEs and iron-group elements (IGEs).² The (reduced) composition of the ashes and the energy release as a function of fuel density is taken from pre-calculated tables (see Appendix A). The adjustment of the nuclear statistical equilibrium (NSE) composition to the changing thermodynamic background state (see Seitenzahl et al. 2009c) and electron captures is also taken into account. As we cannot fully resolve the turbulent structures that have an impact on the flame surface and thus the burning speed, a subgrid-scale turbulence model is applied to determine an effective burning velocity which is valid on our grid scale (for details, see Schmidt, Niemeyer & Hillebrandt 2006a; Schmidt et al. 2006b). For the flame–flow coupling, we use the ‘passive implementation’ described in Reinecke et al. (1999).

² In our hydrodynamic simulations our initial WD composition is represented as $X_{^{12}\text{C}} = 0.5$ and $X_{^{16}\text{O}} = 0.5$ with an electron fraction of $Y_e = 0.49886$, which corresponds to a ^{22}Ne content of 2.5 per cent by mass.

Self-gravity is included using the monopole approximation for the gravitational potential. To test the influence of asymmetries in the gravitational field on our simulation results, two of our models were re-calculated using a fast Fourier transformation-based algorithm for solving the Poisson equation. These calculations are performed on a 512^3 -cells uniform grid tracking the WD expansion and are marked with a suffix ‘FFT’ in the model names.

3.2 Nucleosynthesis post-processing

We determine the detailed nucleosynthetic yields of the ejecta in a post-processing step after the hydrodynamic simulation. To this end, we solve a large nuclear network containing 384 species (ranging up to ^{98}Mo ; see Travaglio et al. 2004) for the trajectories of 10^6 equal mass tracer particles, which are passively advected in the hydrodynamic simulation. We use an updated version of the REACLIB reaction rate library (Rauscher & Thielemann 2000, updated 2009).

3.3 Radiative transfer

For our radiative transfer calculations, the final ejecta density and the final post-processing abundances of the tracer particles (which have irregularly distributed coordinates) are mapped on a 200^3 Cartesian grid in asymptotic velocity space with a smoothed-particle-hydrodynamics-like algorithm that accurately conserves the integrated yields (for details, see Kromer et al. 2010). After further down sampling the data to a 50^3 Cartesian grid (velocity resolution: $400\text{--}600\text{ km s}^{-1}$), we perform a time-dependent 3D Monte Carlo radiative transfer simulation with the *ARTIS* code (Sim 2007; Kromer & Sim 2009). For each model we use 10^8 photon packets and follow 111 logarithmically spaced time steps between 2 and 120 d after explosion ignition. We use the ‘cd23_gf-5’ atomic data set of Kromer & Sim (2009) expanded to include ions up to *vii* for elements heavier than Ca but lighter than Cu. To reduce the computational costs, a grey approximation is used in optically thick cells (cf. Kromer & Sim 2009) and for $t < 3$ d, local thermodynamic equilibrium is assumed.

4 HYDRODYNAMIC EXPLOSION MODELS

4.1 Flame propagation

As mentioned in Section 2, in all of our 14 models, the burning takes place exclusively as subsonic deflagration and is initiated in multiple ignition spots close to the WD’s centre (see Fig. 1). At the

beginning of each simulation, the flame propagates at the laminar deflagration speed. Later, the burning is accelerated by instabilities and the interaction with turbulence. Since the growth of these instabilities is strongly influenced by the deflagration ignition geometry, different models show very different rates of flame spreading and acceleration. In the following discussion of our results, we will mainly focus on the four standard models N1def, N20def, N150def and N1600def (see Figs 2 and 3), which are representative for the whole sample and exemplify most of its variety.

Model N1def is a realization of the simplest case, the ignition of a single spherical bubble at a location slightly off-centre (distance from the origin $r = 36.5$ km and bubble radius $R = 10$ km). Its evolution is illustrated in the left-hand column of Fig. 2 and is a result of the buoyant rise of the hot ashes in the initial burning bubble combined with the propagation due to burning: initially the bubble rises without burning much material (see snapshot at $t = 0.5$ s in the left-hand column of Fig. 2), then it spreads laterally, burning a relatively contiguous volume. However, most of the high-density material in the centre of the WD is left unburnt ($t = 1.0$ s). The buoyant rise of the bubble and the expansion of the star due to the liberation of nuclear energy causes the flame to extinguish before it is able to completely wrap around the unburnt core³ ($t = 1.5$ s). Nevertheless, even after flame extinction the hot ashes continue to expand and spread around the unburnt central parts and finally cover almost the full solid angle ($t = 100$ s, when the ejecta have reached homologous expansion to a good approximation).

Other models with a small number of ignition sparks ($N_k \leq 20$) evolve in a manner similar to N1def. The right-hand column of Fig. 2 shows N20def as an example: due to their separation, most bubbles initially rise up individually without much interaction (see snapshot at $t = 0.5$ s) and neighbouring burning fronts only start to merge in the outer layers (see e.g. $t = 1.0$ s and later). Therefore, apart from the fact that more matter is burnt, the final distribution of burning products is relatively similar to that of N1def. At $t = 1.5$ s, when burning ceases, N20def also shows a Ni-rich outer layer that is wrapped around a central region that is mostly unburnt. However, the greater energy release due to the more complete burning of model N20def compared to N1def also leads to higher expansion velocities in the final ejecta (see $t = 100$ s in Fig. 2). In addition, model N20def has a significantly different inner ejecta structure from N1def: despite having a lower mass of unburnt C/O close to the centre, this material occupies a much bigger volume than in N1def. This behaviour is due to differences in the transfer/redistribution of kinetic energy from the ashes to the unburnt fuel (see Section 5.3 for further discussion of the final ejecta structures) and is closely linked to the occurrence and size of a bound remnant that may form for all models with sparsely ignited deflagrations (see Section 4.3).

In models with many ignition sparks ($N_k \gtrsim 100$, see Fig. 3) both burning and expansion take place much more rapidly than in models with few ignition sparks. The flame evolution is no longer one sided, but large flame structures form in all directions. Due to its larger N_k , model N1600def evolves faster than model N150def, but since it burns less mass, the final ejecta velocities are lower (see Section 4.2 and Fig. 4 for the explosion energetics).

Model N150def shows the typical ejecta structure of a strong deflagration: a limited number of large rising plumes of burnt matter (which often reach out to the highest velocities) and downdrafts of unburnt fuel in between. The centre is dominated by unburnt C/O material. Due to the huge number of ignition spots, model N1600def

contains less unburnt matter in the centre. However, in a realistic multidimensional treatment, deflagration burning is never ‘volume filling’ and always develops downdrafts of unburnt matter between rising burning plumes. Therefore, even in this most extreme model, there are several unburnt fingers of C/O material that reach down to the centre.

4.2 Explosion energetics

Our series of models produces a wide range of explosion energies. Total energies ($E_{\text{tot}} = E_{\text{int}} + E_{\text{kin}} + E_{\text{grav}}$) and nuclear energy releases (E_{nuc}) have been calculated globally for the whole star at $t = 100$ s (see Table 1, Fig. 4). Here, E_{int} , E_{kin} and E_{grav} are the global values of internal, kinetic and gravitational binding energy, respectively. The most energetic explosion model (N150def) releases roughly seven times the energy of the least energetic (N1def). To understand the differences, the temporal evolution of E_{tot} and the energy release rate \dot{E}_{nuc} is shown in Fig. 4. In the upper panel, all curves start from the initial binding energy $E_{\text{bind}} = E_{\text{tot}}(t = 0) = -5.19 \times 10^{50}$ erg. After 1.7 s, deflagration burning has ceased in all models and released the energy $E_{\text{def}} = E_{\text{nuc}}(t = 1.7\text{s})$.⁴ To illustrate how the different speeds of burning and expansion lead to different explosion energies, Fig. 5 shows the distribution of burnt masses over the available fuel densities.

Multispot ignition of SN Ia models has been studied extensively in previous work (e.g. Röpke et al. 2006b). Here, we summarize the main results to explain the energetics within our series of models. We start with effects that lead to the acceleration of the burning. An increase in the number of ignition kernels N_k causes: (i) a growth of the initial flame surface area; (ii) an increase of the buoyancy force on the dominating outermost flame features (as r_{max} grows with N_k for our standard models);⁵ and (iii) the excitation of more modes of instabilities that produce turbulence and increase the flame surface. All these effects cause a faster evolution/acceleration of the dominant flame features and thus an increase in \dot{E}_{nuc} with N_k (see Fig. 4a). As the burning competes with WD expansion, an increase in \dot{E}_{nuc} leads to a greater amount of burnt mass at all densities (see Fig. 5a) and a higher deflagration energy E_{def} .

In contrast to these accelerating effects, for large N_k , \dot{E}_{nuc} and E_{def} decrease again due to (iv) early flame surface destruction (if neighbouring flame structures are very close to each other and merge quickly) and (v) rapid early WD expansion. Consequently, for low to intermediate N_k , E_{def} increases, reaches a maximum at $N_k = 150$ and decreases again for $N_k > 150$. Around $N_k = 150$, the growth of the flame is well balanced with the rate of stellar expansion: roughly equally sized flame structures are distributed over the whole solid angle, which maximizes the amount of matter burnt (cf. Röpke et al. 2006b). Note that our optimum number of ignition sparks differs significantly from the value found by Röpke et al. (2006b) (150 kernels *per octant*), as they used ignition kernels with a smaller radius $R_k = 5$ km (this study uses $R_k = 10$ km in all

⁴ In models with a bound remnant, some more burning occurs at later times during the pulsations of the remnant, as our level set based burning scheme is not turned off and still releases some energy if the (former) flame front is advected to or shocked to high densities.

⁵ The buoyancy force increases with the effective gravitational acceleration at the location of the bubble and with the bubble size (see, e.g. Röpke et al. 2006b, for further details). In the inner parts of our WDs, the absolute value of the gravitational acceleration increases with radius (see Fig. 6b).

³ The extinction density for C/O deflagrations is $\sim 5 \times 10^6$ g cm⁻³.

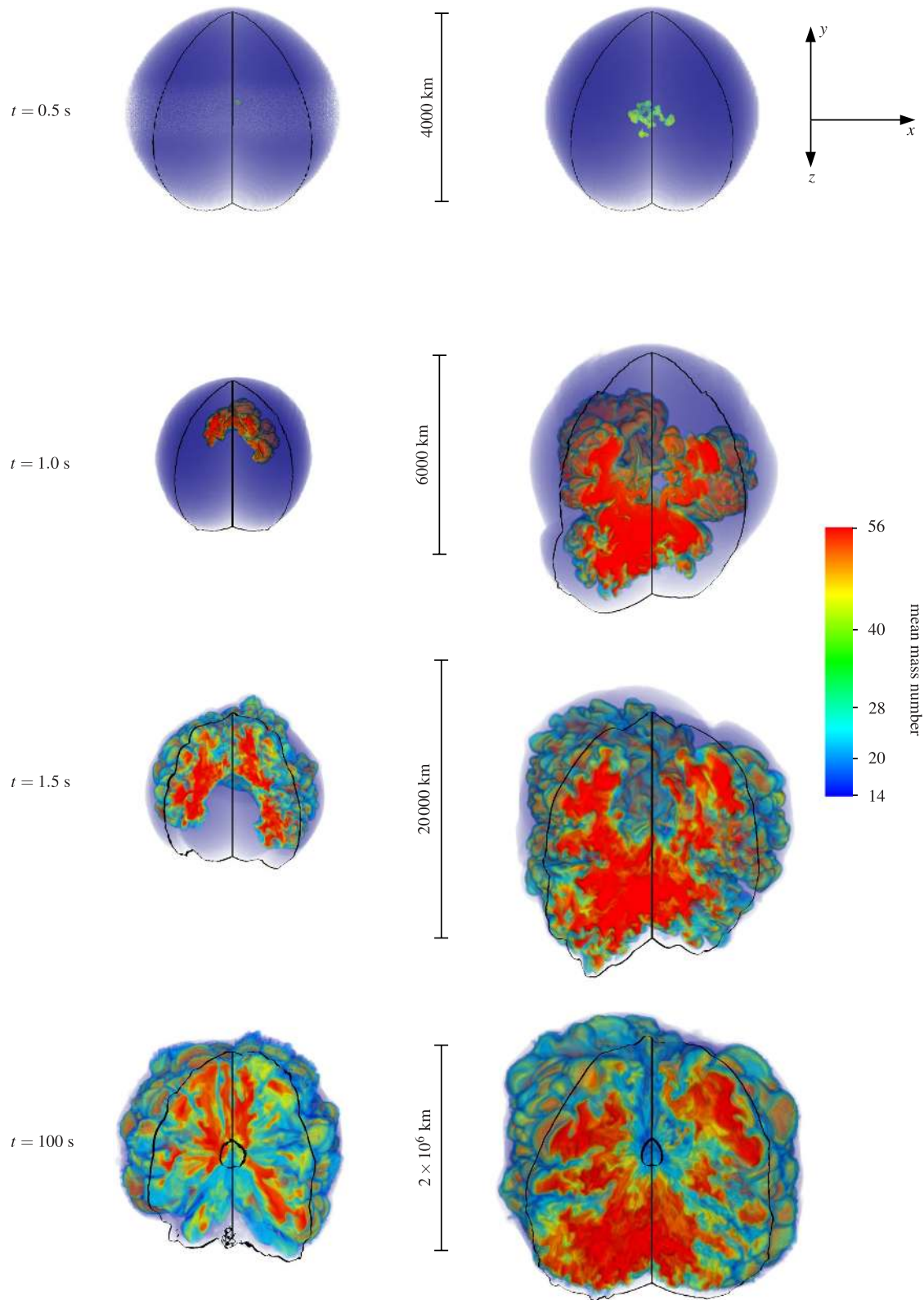


Figure 2. Explosion evolution for models N1def (left-hand column) and N20def (right-hand column). Colour coded is the mean mass number calculated from the reduced set of species in the hydrodynamic simulation. In the volume renderings a 90° wedge is cut out in the front part of the ejecta. The times after explosion initiation are from top to bottom: $t = 0.5$, 1.0, 1.5 and 100 s (for each time the length-scale along the middle axis of the plots is given in the centre). At $t = 100$ s, the innermost black contours mark the outer edges of the regions which do not become gravitationally unbound.

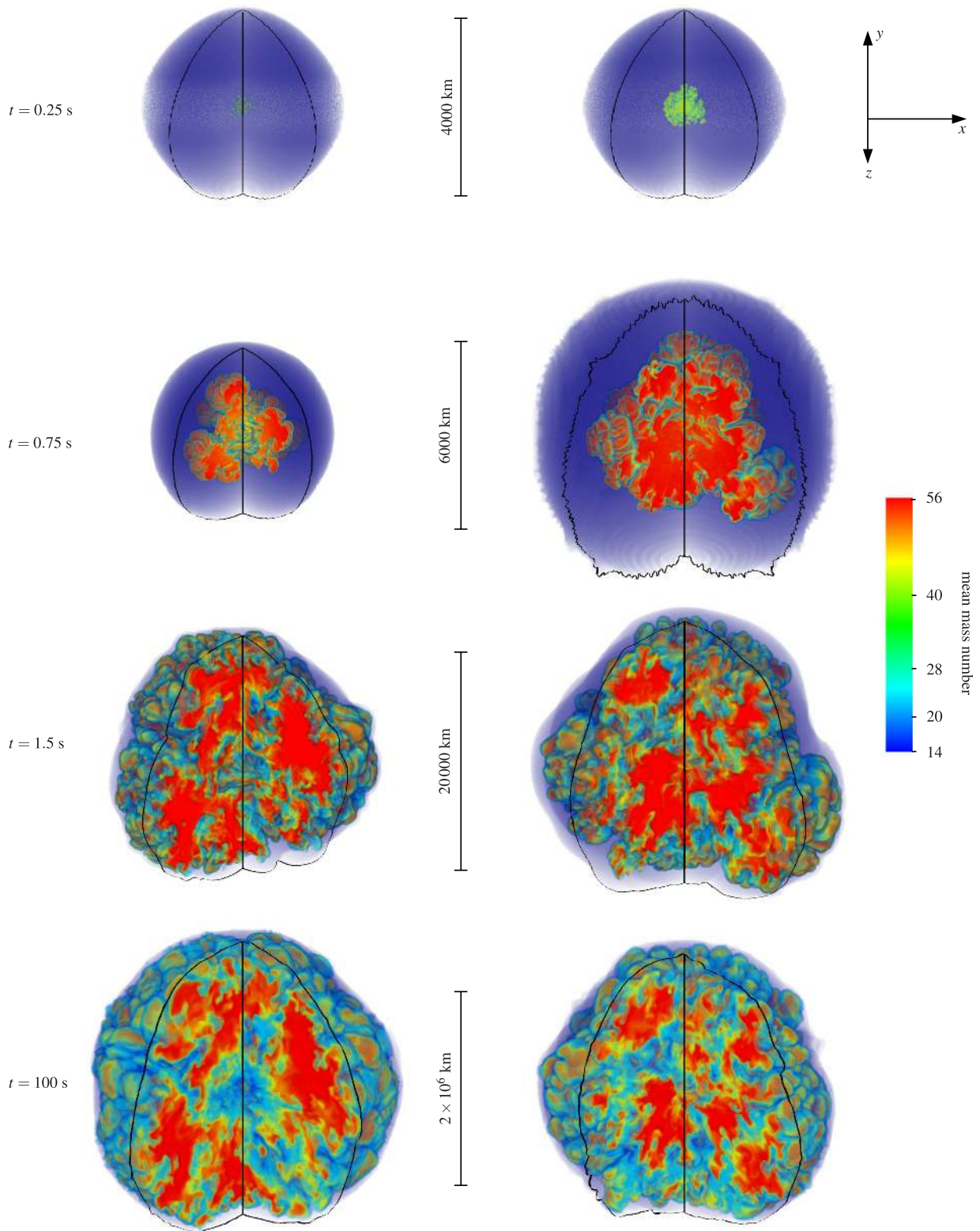


Figure 3. As Fig. 2, but showing models N150def (left-hand column) and N1600def (right-hand column). The times after explosion initiation are from top to bottom: $t = 0.25, 0.75, 1.5$ and 100 s.

models except N300Cdef). Fig. 5(a) shows that at high densities models with very high N_k burn more than N150def, but at low densities they burn significantly less. Despite these differences, as in Röpke et al. (2006b), all vigorously ignited models fall into a nar-

row range of E_{tot} around 6×10^{50} erg at the end of the deflagration phase.

In models with *compact* ignition configuration (dotted and dashed lines in Fig. 4), the same number of ignition kernels is located within

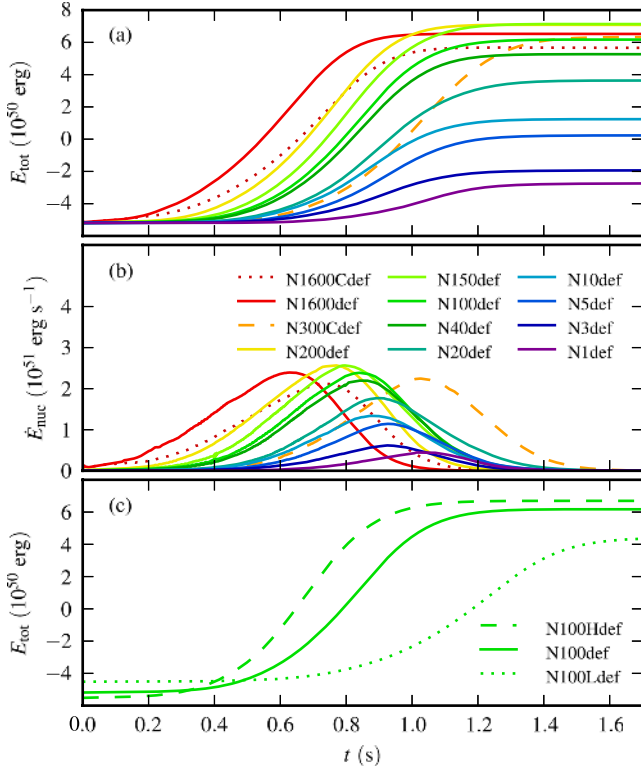


Figure 4. Temporal evolution of total energy (a) and rate of nuclear energy release (b) for all models with our standard initial WD model ($\rho_c = 2.9 \times 10^9 \text{ g cm}^{-3}$) in the initial 1.7 s. The total energy evolution for the N100 deflagration models with different WD central densities is shown in panel (c).

a smaller volume compared to the other models in our sequence. Model N1600Cdef has lower \dot{E}_{nuc} and E_{def} than N1600def, due to reduced buoyancy forces (ii) and even more severe flame surface destruction (iv). For model N300Cdef, both the significantly lower value of r_{max} and the lower ignition kernel radius, $R_k = 5 \text{ km}$ (half the value of the other models) lead to very low buoyancy forces (ii)

Table 1. Total masses (in solar masses) of the ejecta, the bound remnants and the main ejected nucleosynthesis products and explosion energies (in units of 10^{50} erg) of all models.

Model	M_{ej}	M_{b}	$M_{^{56}\text{Ni}}$	M_{IGE}	M_{IME}	$\frac{M_{^{56}\text{Ni}}}{M_{\text{IGE}}}$	$\frac{M_{\text{IGE}}+M_{\text{IME}}}{M_{\text{ej}}}$	E_{nuc}	$\frac{E_{\text{nuc}}}{ E_{\text{bind}} }$	E_{tot}	$E_{\text{kin,ej}}$
N1def	0.0843	1.32	0.0345	0.0468	0.00893	0.74	0.66	1.74	0.34	-0.580	0.149
N3def	0.195	1.21	0.0730	0.106	0.0257	0.69	0.68	3.06	0.59	-0.104	0.439
N5def	0.372	1.03	0.158	0.222	0.0416	0.71	0.71	4.90	0.94	0.962	1.35
N10def	0.478	0.926	0.183	0.267	0.0581	0.69	0.68	5.87	1.1	1.68	1.95
N20def	0.859	0.545	0.264	0.394	0.125	0.67	0.60	8.36	1.6	3.68	3.75
N40def	1.21	0.190	0.335	0.509	0.142	0.66	0.54	10.2	2.0	5.26	5.22
N100Ldef	1.23	0.133	0.326	0.413	0.138	0.79	0.45	8.79	1.9	4.36	4.32
N100def	1.31	0.090	0.355	0.545	0.147	0.65	0.53	11.1	2.1	6.16	6.11
N100Hdef	1.31	0.102	0.329	0.576	0.179	0.57	0.58	11.8	2.1	6.68	6.63
N150def	1.40	(0.048)	0.378	0.583	0.164	0.65	0.53	12.1	2.3	7.12	6.98
N200def	1.40	(0.021)	0.371	0.598	0.146	0.62	0.53	12.0	2.3	7.07	6.95
N300Cdef	1.40	(0.027)	0.334	0.526	0.167	0.63	0.50	11.2	2.2	6.31	6.26
N1600def	1.40	(0.016)	0.340	0.582	0.132	0.58	0.51	11.5	2.2	6.50	6.38
N1600Cdef	1.40	(0.016)	0.315	0.532	0.136	0.59	0.48	10.7	2.1	5.63	5.50

M_{ej} and M_{b} are the total masses of the ejecta and the bound material; $M_{^{56}\text{Ni}}$, M_{IGE} and M_{IME} are the ejected masses of ^{56}Ni , IGEs and IMEs (as determined in the nucleosynthesis post-processing). The small bound masses (values in brackets) of vigorously ignited models were neglected and considered as part of the ejecta. $E_{\text{kin,ej}}$ is the asymptotic kinetic energy of the ejecta, the other energy values are calculated for the whole WD.

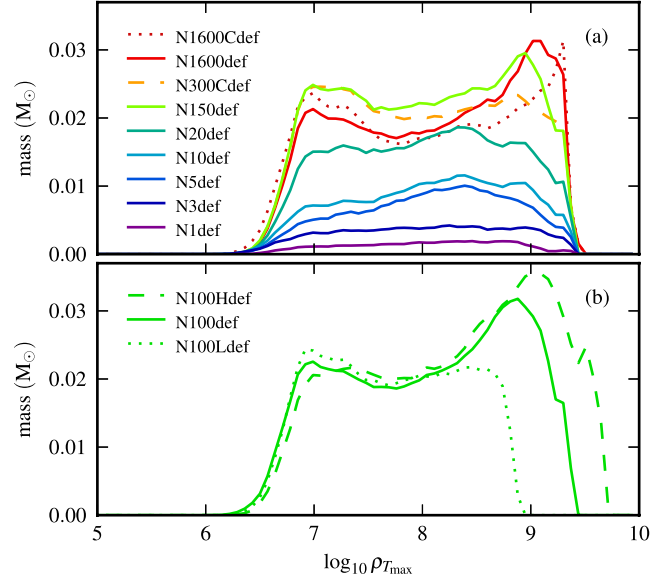


Figure 5. Distribution of ejected mass as a function of the density at which it was burnt ($\rho_{T_{\text{max}}}$ is the density at the maximum temperature experienced by a tracer particle): (a) for select models with $\rho_c = 2.9 \times 10^9 \text{ g cm}^{-3}$ and (b) for the N100 deflagration models with different central densities.

and cause the burning in this model to evolve significantly more slowly than in all others. However, the smaller value of R_k allows the bubbles that are initially burning to rise before they merge with their neighbours. As a result, the ignition configuration eventually evolves to a state similar to that in the less compact configurations (e.g. N100def) and the total energy release is comparable.

Recently, Long et al. (2013) have also studied 3D deflagration models based on multispot ignition setups. They find that their models with fewer ignition kernels reach higher explosion energies than those with more ignition kernels. This relation holds only because most of their setups with large N_k are ‘saturated’: they place as many ignition kernels into the ignition volume as possible without intersection. Thus, effects of early flame surface destruction (iv) and rapid early expansion (v) are very pronounced and lead to relatively

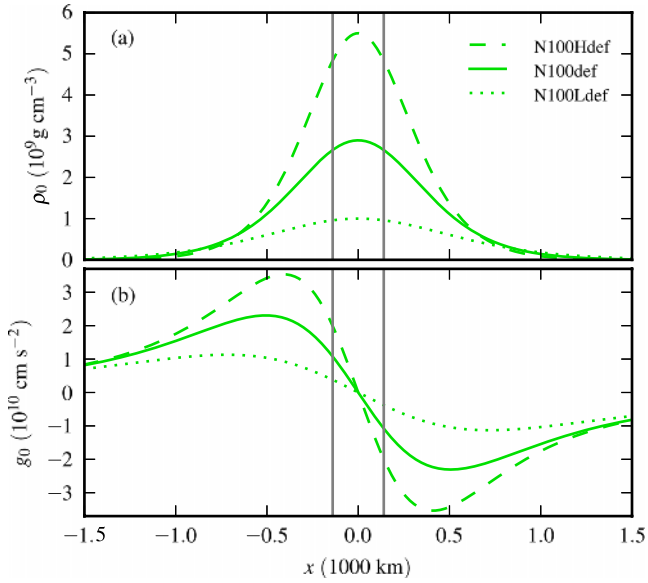


Figure 6. Initial density profiles (a) and gravitational acceleration (b) of the N100 deflagration models with different central densities. The ignition kernels are located between the two vertical grey lines.

low values of E_{def} . Among their models with non-saturated setups, however, similar trends hold as for our set of models (E_{def} increases from $N_k = 63$ to 128 and then decreases again for $N_k = 1700$). Most of the setups in our study are far from being saturated.

We have studied the importance of the central density for the N100 ignition geometry (see Fig. 6 for a comparison of the three density profiles and the location of the ignition kernels). The main difference of the ‘H’ (‘L’) version is that the deflagration starts off at significantly higher (lower) densities and that there is more (less) high-density material available for burning. This is directly reflected in the density distribution of burnt matter (see Fig. 5b): with respect to N100def, the right peak in the H (L) model shifts to higher (lower) densities, whereas the low-density side of the distribution does not show significant changes. Dynamically, the increased (decreased) mass that sits at $r < r_{\text{max}}$ leads to an increase (decrease) of the gravitational acceleration (see Fig. 6b) and thus to more (less) buoyancy. Consistently, the flame evolves faster for higher central densities (see Fig. 4c). Combined with the higher amount of fuel at higher density, this also leads to higher deflagration energies E_{def} . While the L model has a significantly lower final E_{def} than the standard model, an increase of the central density (as in the H model) does not yield a substantial increase of E_{def} .

4.3 Unbinding the white dwarf star

Deflagrations can leave a considerable mass of high-density unburnt fuel close to the centre of the WD. This material is not accelerated to high speeds in the course of the explosion. If, in the end, the velocity of a volume element within this matter does not reach the escape velocity with respect to the mass that sits at lower radii, it stays bound and is not ejected. To determine which part of the WD becomes unbound, we have calculated the asymptotic specific kinetic energy, $\epsilon_{\text{kin,a}}$, as the sum of the specific gravitational and

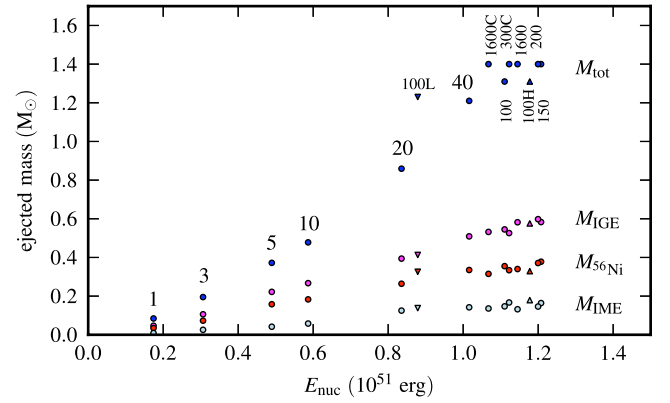


Figure 7. Total ejected masses and IGE, ^{56}Ni and IME masses among the ejecta versus nuclear energy release in the explosion. Models with ≤ 100 ignition sparks leave a compact remnant.

kinetic energies for each cell on our hydrodynamic grid at the end of the simulation.⁶

$$\epsilon_{\text{kin,a}} = \epsilon_{\text{grav}}(100 \text{ s}) + \epsilon_{\text{kin}}(100 \text{ s}). \quad (1)$$

For $\epsilon_{\text{kin,a}} > 0$, a cell becomes unbound and will eventually approach the asymptotic velocity

$$v_a = \sqrt{2\epsilon_{\text{kin,a}}}. \quad (2)$$

If $\epsilon_{\text{kin,a}} \leq 0$, the cell will be left behind after the explosion and stay in a bound remnant. Note that models with similar total energy release can have significantly different ejecta masses since it is crucial where the explosion energy is deposited.

We have determined ejecta masses M_{ej} and masses of the bound remnants M_b for all of our models (see Table 1 and Fig. 7). Models with many ignition kernels ($N_k > 100$) release a large amount of energy and deposit sufficient energy close to the centre (e.g. by transferring kinetic energy to the downdrafts of unburnt fuel) to unbind the whole WD, including the central unburnt fuel. In the case of a low or intermediate number of ignition sparks ($N_k \lesssim 100$), only part of the WD becomes unbound. Most of the unburnt fuel remains in the remnant, while the ejected part reaches homologous expansion. We find a continuum of remnant masses between 1.32 and $0.09 M_{\odot}$ and, as Fig. 7 shows, a monotonic (roughly linear) increase of M_{ej} with the nuclear energy release E_{nuc} below $E_{\text{nuc}} \sim 1.1 \times 10^{51}$ erg (or for $N_k < 100$). Table 1 also gives the values of the asymptotic kinetic energies of the ejecta. Further properties of the remnants are discussed in Section 4.5.

4.4 Pulsations/chances of a secondary detonation?

As reported by other recent studies (Bravo & García-Senz 2009; Jordan et al. 2012b), the weak deflagrations in our model series also lead to pulsations within the WDs: Fig. 8 shows that the burning causes significant expansion (seen in the figure as a decrease in the temporal evolution of the maximum density). For models with low N_k , the bound inner parts start to contract after the deflagration has ceased. After maximum compression, the dense core region starts to expand again, while outer parts are still falling inwards. Thus, an accretion shock forms somewhere near the edge of the dense

⁶ We have neglected any potential contribution of the internal energy here. Its inclusion does not lead to a significant decrease of the bound masses (at most 1.8 per cent) of our model sample.

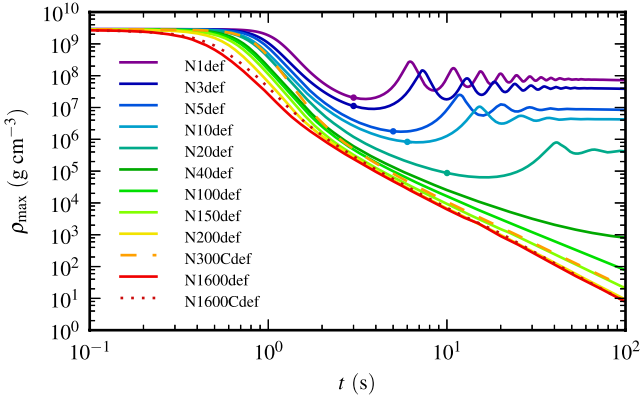


Figure 8. Maximum density ρ_{\max} on the hydrodynamic grid as indicator for the temporal evolution of expansion and pulsations. For the five weakest deflagration models, the evolution of ρ_{\max} at late times was determined in separate simulations in which the grid expansion was stopped to keep the bound remnants spatially resolved (parts of the curves after the circle marks).

core (for a more detailed description, see e.g. Bravo & García-Senz 2009) and some matter around this shock region is heated up significantly. Shortly thereafter, the infall is stopped and all matter is again moving outwards, but, as it is still gravitationally bound, further pulsations ensue with steadily decreasing amplitudes. The weaker the strength of the deflagration and the more massive the bound remnant of a model, the more violent are these pulsations.

Previous studies found that the high temperatures in the accretion shock may be sufficient to trigger a secondary detonation for $E_{\text{nuc}} \lesssim E_{\text{bind}}$ (Bravo & García-Senz 2009). Since the ignition occurs at the radius of the accretion shock, Bravo & García-Senz call this scenario pulsating reverse detonation (PRD). If the deflagration is very one sided, however, even before the formation of an accretion shock, a hotspot may form due to the deflagration ashes converging on the opposite side of the ignition. This so-called classical GCD scenario typically works for low deflagration energies with $E_{\text{nuc}} \sim 0.1E_{\text{bind}}$ (Jordan et al. 2012a). For slightly stronger deflagrations (which cause significant stellar expansion in the early burning stages), the conditions may be insufficient for detonation initiation at this point. But, as Jordan et al. (2012a) report, for E_{nuc} within $0.38\text{--}0.78E_{\text{bind}}$, the compression at the onset of the first pulsation may be sufficient to increase both temperature and density in the hotspot to the critical values (see Röpke, Woosley & Hillebrandt 2007a; Seitenzahl et al. 2009b). This so-called pulsationally assisted GCD will likely precede a potential PRD.

In our series of models, we do not find conditions suitable for any secondary detonation for models with $N_k \geq 5$. Model N5def just reaches 10^9 K in the accretion shock, but only at densities which are too low for detonation initiation ($\rho < 10^6$ g cm $^{-3}$). All stronger deflagrations ($N_k \geq 10$) do not even reach temperatures of 10^9 K, which would be necessary for detonation. For our weakest deflagration models N1def and N3def, we cannot exclude a secondary detonation. Their explosion energies of 0.34 and $0.59E_{\text{bind}}$ could make them candidates for potential pulsationally assisted GCDs or PRDs. However, as we find conditions that are only marginally critical (according to Röpke et al. 2007a; Seitenzahl et al. 2009a), only future studies with simulations designed to sufficiently spatially resolve the relevant regions can provide an answer. Here, we focus on the outcomes of pure deflagration models.

Table 2. Centre-of-mass kick velocities of the bound remnants.

Model	v_{kick} (km s $^{-1}$)	Model	v_{kick} (km s $^{-1}$)
N1def	5.1	N10def	6.8
N1def_FFT	8.2	N20def	18
N3def	4.4	N40def	32
N5def	5.4	N100def	16
N5def_FFT	36		

4.5 Properties of the remnant object

As discussed in Section 4.3, our weakest deflagrations leave behind bound remnants with masses given in Table 1. Both the remnant mass and the strength of the pulsations increase with decreasing nuclear energy release of the deflagration. After the first and strongest pulsation, a dense nearly hydrostatic (cf. Bravo & García-Senz 2009) core forms within the bound material. This core, which is heated in the pulsations and the accretion shock, is similar to a very hot WD and contains most of the bound mass. The outer layers of the core are already enriched with deflagration ashes as the innermost burnt regions have never become unbound. The bound mass outside the core is also a mix of deflagration ashes and unburnt fuel; it may eventually settle down on the hydrostatic core. For a detailed description of the nucleosynthetic yields in the bound remnants, see Section 5.2.

In asymmetric explosions that leave remnants, a recoil momentum of the remnant may be expected. Jordan et al. (2012b) report a high kick velocity of a few hundred km s $^{-1}$ for their deflagration models that were ignited at off-centre points. Such strong kicks could be sufficient to eject the remnants from the system and produce potentially observable runaway/hypervelocity WDs. However, in our study we do not find such high kick velocities (see Table 2): our values are at maximum 5 to 10 per cent of the values in Jordan et al. (2012b). This might be partially due to a higher degree of asymmetry in the ignition setups of Jordan et al. (compared to our sparsely ignited models), who ignite (in most cases) relatively large off-centre volumes of radius 128 km. On the other hand, our monopole gravity solver, which is used in most models, could suppress higher kick velocities. To test the role of the gravity solver, we have re-simulated our models N1def and N5def using a fast Fourier transformation-based gravity solver that solves the full 3D Poisson equation without approximations (see Section 3.1). Currently, this solver is restricted to uniform grid geometries. Thus, these models have a lower spatial resolution of the inner parts of the WD than our other models (which use a hybrid grid; see Section 3.1). Due to the lower spatial resolution of the initial flame, these new models N1def_FFT and N5def_FFT release somewhat less energy in the explosion, but qualitatively they agree well with the corresponding monopole gravity simulations and the large-scale flame evolution and asymmetry are very similar. Regarding the kick velocity, only N5def_FFT has a noticeably higher value (36 km s $^{-1}$), but this is still roughly of an order of magnitude lower than the values found by Jordan et al. (2012b). The main results of this work, namely the nucleosynthesis and the observable predictions for the ejected matter should, however, not depend on a potential recoil.

5 NUCLEOSYNTHESIS

In this section, we discuss the results of our detailed nucleosynthesis post-processing calculations (see Section 3.2). We first cover the total integrated yields within the ejecta and the remnant objects

(Sections 5.1 and 5.2) and then present the detailed geometrical structures of the ejected nucleosynthetic yields in velocity space (Section 5.3).

5.1 Total nucleosynthetic yields in the ejecta

Global yields of stable and radioactive nuclei in the ejecta are shown in Tables B1 and B2 in the Appendix. For a quick overview, yields of the most important (classes of) species are also given in Table 1 and plotted in Fig. 7.

As shown in Fig. 7 and explained in Section 4.2, for $N_k \leq 150$ the nuclear energy release E_{nuc} increases with the number of ignition bubbles N_k ; for larger N_k , E_{nuc} decreases. The mass of ^{56}Ni produced scales with E_{nuc} and also follows these trends. The maximum ^{56}Ni mass of $0.38 M_{\odot}$, which is produced in model N150def, is marginally compatible with the lower end of the distribution of ^{56}Ni masses reported for normal SNe Ia (cf. e.g. Stritzinger et al. 2006). Neutronization by electron captures is only efficient at the highest burning densities. Consequently, the degree of neutronization increases with N_k in our model series since, as shown in Fig. 5(a), models with higher N_k burn more mass at the highest fuel densities. The ratio of the mass of $M_{^{56}\text{Ni}}$ (which has equal numbers of protons and neutrons) to the total mass of IGEs that is produced in NSE thus also goes down with N_k (see Table 1). Models N100Ldef and N100Hdef are outliers from this general trend: due to their lower/higher central densities, they have a lower/higher degree of neutronization and thus ^{56}Ni masses that lie slightly above/below the mean trend in Fig. 7 (see also Seitenzahl, Ciaraldi-Schoolmann & Röpke 2011). The total mass of IMEs (e.g. ^{28}Si , ^{32}S) is roughly 20 to 30 per cent of the total mass of IGEs. One of the less obvious results is the decrease of the amount of burning products (estimated roughly by $\frac{M_{\text{IGE}} + M_{\text{IME}}}{M_{\text{ej}}}$ in Table 1) within the ejecta from weak to strong deflagrations: the mass fraction of burning products ranges from about 70 down to only 50 per cent. This occurs because, for weak deflagrations, a large fraction of the unburnt fuel becomes part of the bound remnant and is thus not released into the ejecta.

5.2 Nucleosynthetic yields in the bound remnant

Total integrated nucleosynthetic yields of stable and radioactive nuclei in the bound remnants are given in Tables B3 and B4 in the Appendix. An overview of the composition is provided in Table 3: as previously reported by Jordan et al. (2012b) and discussed in Section 4.5, the bound remnants produced in the weak deflagration models are enriched by products of the explosive burning (mainly in the outer layers). If we count only IGEs and IMEs, these products contribute 3–10 per cent to the remnant mass (see Table 3). After

cooling down, the remnant objects will again become WDs, but with very peculiar composition.

In addition to the deflagration products, some oxygen and neon might also have been produced by carbon burning during the pulsations of the central regions (densities are too low to reach NSE). In this study, we have not incorporated the energy release of this burning phase correctly in the hydrodynamic simulations and so may somewhat underestimate the burning yields in our post-processing (see, however, footnote 4).

As discussed in detail by Kromer et al. (2013), radioactive material in the outer layers of the bound remnants may explain the relatively slowly declining light curves and peculiarities in the late-time spectra of 2002cx-like SNe (Jha et al. 2006; Phillips et al. 2007). Currently, radioactive decays in the bound remnants are not taken into account by our radiative transfer simulations.

5.3 Velocity distribution of ejected yields

The distribution of nucleosynthetic yields in velocity space and the underlying density profile determine the observable outcomes of the explosion. We have calculated synthetic light curves and spectra for our models (see Section 6). For a better understanding of the results, we describe the most important properties of the nucleosynthetic yield distributions here.

Fig. 9 shows the final abundance distributions of select species and the density in 2D slices in asymptotic velocity space. Again, we focus our discussion on the four models N1def, N20def, N150def and N1600def, which are representative for the whole sample and its variety (see Fig. 10 for spherically averaged distributions). The distributions show complex multidimensional structures typical for deflagration models. The outer contours of the ashes of the main burning plumes are most clearly visible in the ^{12}C abundance plots (as regions where carbon is absent; cf. also the final snapshots in Figs 2 and 3). Inside the ash-rich regions, the typical products of burning in C/O matter are found: at the outer edges, incomplete burning leads to the production of ^{16}O and IMEs including ^{28}Si (which is nowhere very prominent). The main burning products are, however, IGEs. The stable IGEs, which are mostly neutron rich, are produced in the initial stages of the deflagration, when the burning bubbles are still located at the high-density regions close to the centre. Heated by the burning, the ashes (and also surrounding unburnt fuel) rise up through buoyancy. In this way, the burning at the edges of the deflagration plumes burns the matter only after some pre-expansion. At these lower densities, the freeze-out composition from NSE is mainly ^{56}Ni . Therefore, the ^{56}Ni in the distribution plots mostly surrounds the regions rich in stable IGEs. Due to the inhomogeneous growth and structure of the deflagration plumes, there are also inhomogeneities in the distribution of IGEs. Only

Table 3. Composition of the bound remnants (masses in solar masses).

Model	M_b	$M_{^{56}\text{Ni}}$	M_{IGE}	M_{IME}	$M_{^{20}\text{Ne}}$	$M_{^{16}\text{O}}$	$M_{^{12}\text{C}}$	$\frac{M_{^{56}\text{Ni}}}{M_{\text{IGE}}}$	$\frac{M_{\text{IGE}} + M_{\text{IME}}}{M_b}$
N1def	1.32	0.0325	0.0417	0.0354	0.0448	0.622	0.547	0.78	0.058
N3def	1.21	0.0159	0.0230	0.0391	0.0461	0.578	0.497	0.69	0.051
N5def	1.03	0.0221	0.0305	0.0352	0.0345	0.486	0.424	0.72	0.064
N10def	0.926	0.0214	0.0296	0.0413	0.0360	0.432	0.369	0.72	0.077
N20def	0.545	0.004 45	0.006 21	0.0175	0.0235	0.261	0.225	0.72	0.044
N40def	0.190	0.000 80	0.001 26	0.004 04	0.008 72	0.0921	0.0799	0.63	0.028
N100Ldef	0.133	0.002 62	0.003 18	0.003 49	0.000 74	0.0637	0.0584	0.82	0.050
N100def	0.090	0.000 76	0.001 05	0.001 99	0.002 02	0.0437	0.0392	0.73	0.034
N100Hdef	0.102	0.000 38	0.000 61	0.009 55	0.0181	0.0462	0.0258	0.63	0.10

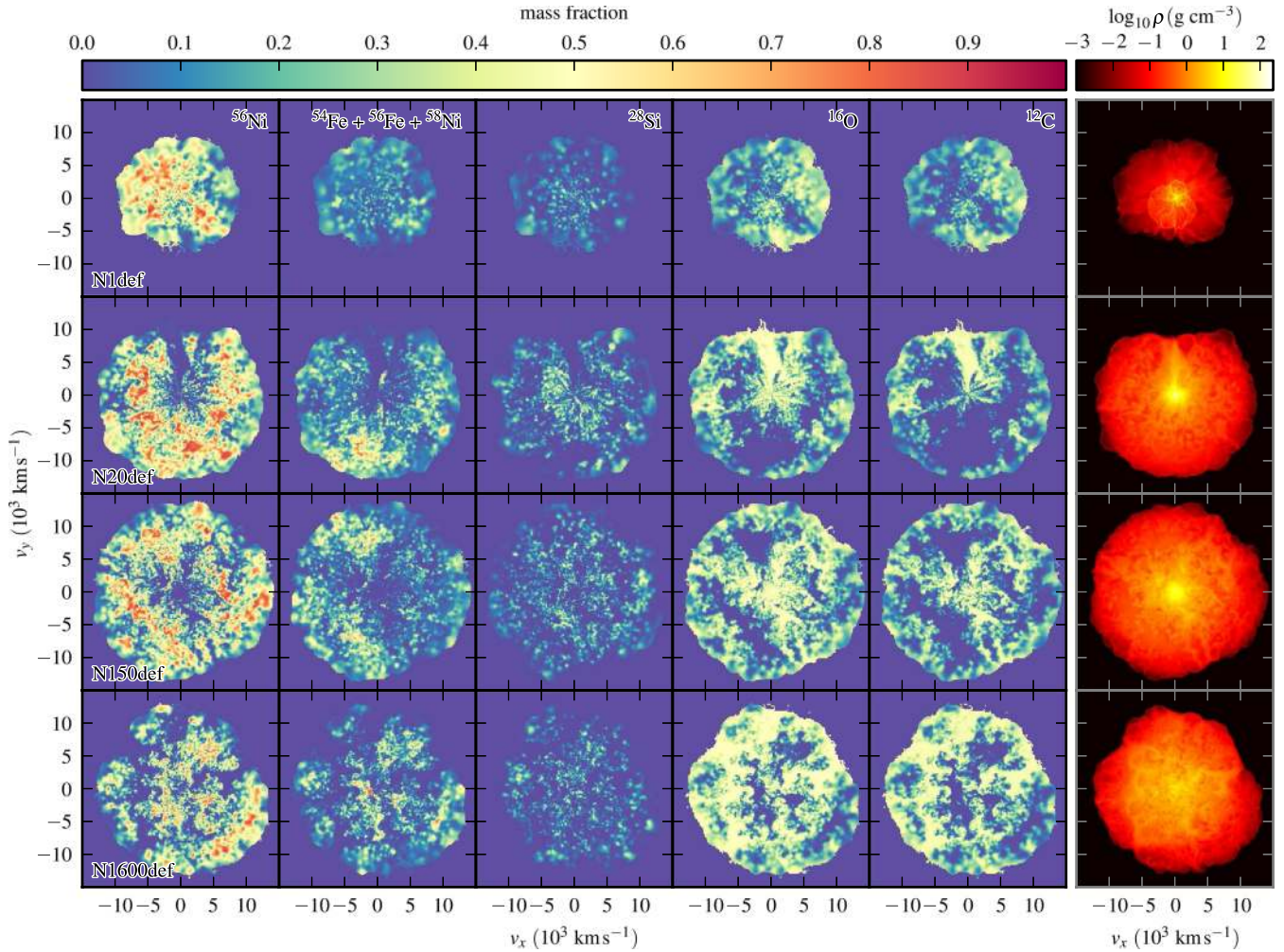


Figure 9. Slices through the mid-plane of the final ejecta distributions of the models N1def, N20def, N150def and N1600def (top to bottom) in asymptotic velocity space (i.e. only material reaching escape velocity is shown). Colour coded are the mass fractions of ^{56}Ni , the sum of the most abundant stable IGEs (^{54}Fe , ^{56}Fe and ^{58}Ni), the IME ^{28}Si , the remaining ^{16}O and ^{12}C fuel and $\log_{10}\rho$ (left to right). The abundance distributions have been calculated by mapping the tracer particle distributions on to a 200^3 Cartesian grid as described in Section 3.3. For the density, the cells of the hydrodynamic grid that reach escape velocity have been mapped in the same way as the tracer particles.

if all IGEs are summed do the large contiguous red areas seen in Figs 2 and 3 become visible.

Between the burnt structures, the ejecta are filled with unburnt material that has sunk down between the burning bubbles or has expanded less than the hot ashes. As discussed above, one-sided deflagrations (typical for low N_k) tend to extinguish before the burning front can completely wrap around the outer layers of the whole star. Therefore, a channel of unburnt matter that reaches from the ejecta surface down to the centre is present in several models (e.g. N20def). Models with intermediate numbers of ignition sparks ($N_k \sim 40\text{--}150$) tend to have relatively few large equally sized contiguous burning plumes. Unburnt fuel is found mainly close to the centre and in thin channels between the plumes. Models with larger numbers of ignition sparks ($N_k \geq 200$) tend to have a greater number of smaller burning plumes. Regions of unburnt fuel occupy a very large volume and are most prominent in the outer parts of the ejecta (thus models like N1600def show large mass fractions of unburnt fuel at high velocities in Fig. 10). For all models, the unburnt structures can also be seen as regions with slightly higher density than neighbouring burnt material, as they have expanded less (rightmost panels of Fig. 9). In model N1def (and the other

models with $N \leq 10$) the former accretion shock of the most violent pulsation is still visible as asymmetric shell-like structure with a jump in density.

Despite the small-scale asymmetries due to turbulent mixing, the large-scale asymmetries of the final ejecta structures are only moderate. Often, asymmetries during the early burning stages are mitigated later, when the burning plumes expand into unburnt regions. As explained above, sparsely ignited one-sided deflagrations tend to be especially asymmetric and models with intermediate N_k are more symmetric than all other models. Observable consequences of such large-scale asymmetries will be discussed in Section 6.3.

In the complex 3D structures of our deflagration models, burning products such as ^{56}Ni , stable IGEs and IMEs and also unburnt ^{12}C and ^{16}O can be found at all ejecta velocities. Spherical averages of our models show low maximum ejecta velocities v_{max} in the range $9000\text{--}15000 \text{ km s}^{-1}$ (see Figs 10 and 11). The distribution of v_{max} simply follows that of the (low) explosion energies (see Section 4.2 and Fig. 7). We caution that spherical averages suggest that the ejecta are very homogeneously mixed, which is, as we have just seen, not really the case in multidimensional space.

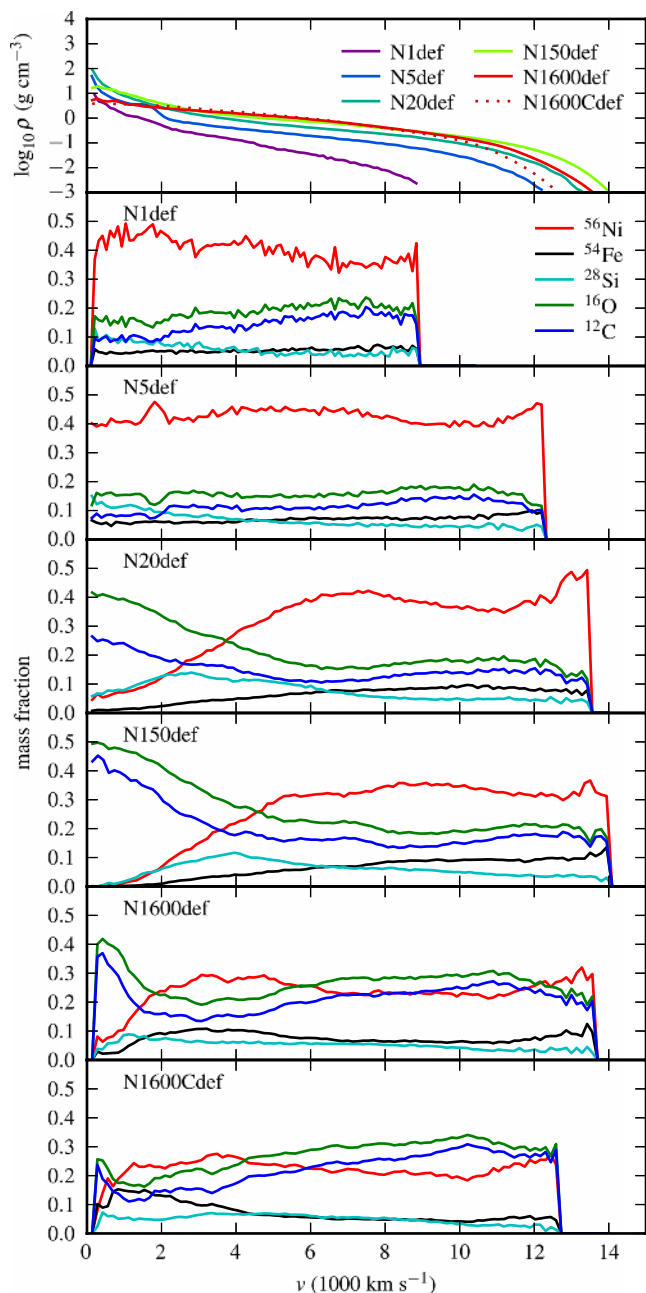


Figure 10. Angle-averaged density and composition in asymptotic velocity space (i.e. only material reaching escape velocity is shown). For the averaging, 100 radial bins were used.

In the weakest deflagration models, most of the unburnt material is not ejected. This unburnt material becomes part of the bound remnant. Therefore, these models have a particularly homogeneous abundance distribution in the ejecta (see models N1def and N5def in Fig. 10).

In models for which the ejected mass exceeds the bound mass ($N_k \geq 20$), unburnt material becomes increasingly dominant in the central ejecta. ^{56}Ni and other IGEs are relatively scarce in these central ejecta. The adjacent layer with an almost homogeneous mix of fuel and deflagration ashes (as seen in N1def and N5def) is shifted towards higher velocities, compared to the weaker models.

For models with increasing deflagration strength (and N_k up to 150), the central region that is dominated by unburnt C/O material

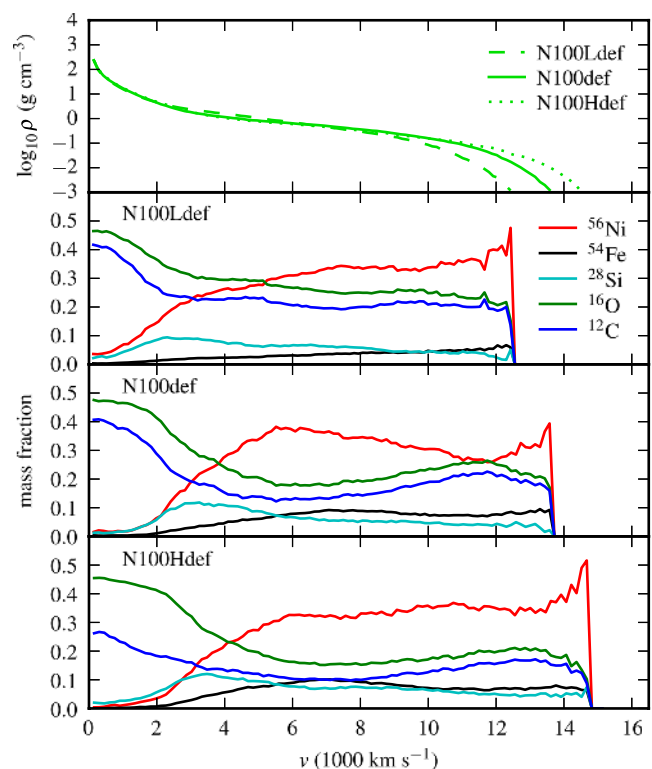


Figure 11. Same as Fig. 10, but for the N100 deflagration models with different central densities.

extends to higher velocities. For models with $N_k \geq 200$, however, the amount of unburnt matter in the centre decreases, as more and more high-density material is burnt in the earliest burning stages (see Section 4.2, Fig. 5a). Accordingly, the fraction of stable IGEs is increased and extends down to the lowest velocities. This behaviour might be a side effect of our parametrization of the deflagration strength with the multispot ignition scenario.

Partially bound models show a characteristic peak at the centre in their density profile, whereas fully unbound models with $N_k \gtrsim 200$ are flat. This is consistent with the enhanced nuclear burning and energy deposition of these models at the highest densities.

The variation of the central density in models with the N100 ignition geometry has only a moderate influence on the final ejecta structure (Fig. 11). The qualitative changes for increasing ρ_c are similar to the changes for increasing N_k along our series (for intermediate N_k).

6 SYNTHETIC OBSERVABLES

In this section, we present synthetic light curves and spectra for our models as obtained from radiative transfer calculations with the ARTIS code (for a description of the simulation setup see Section 3.3).

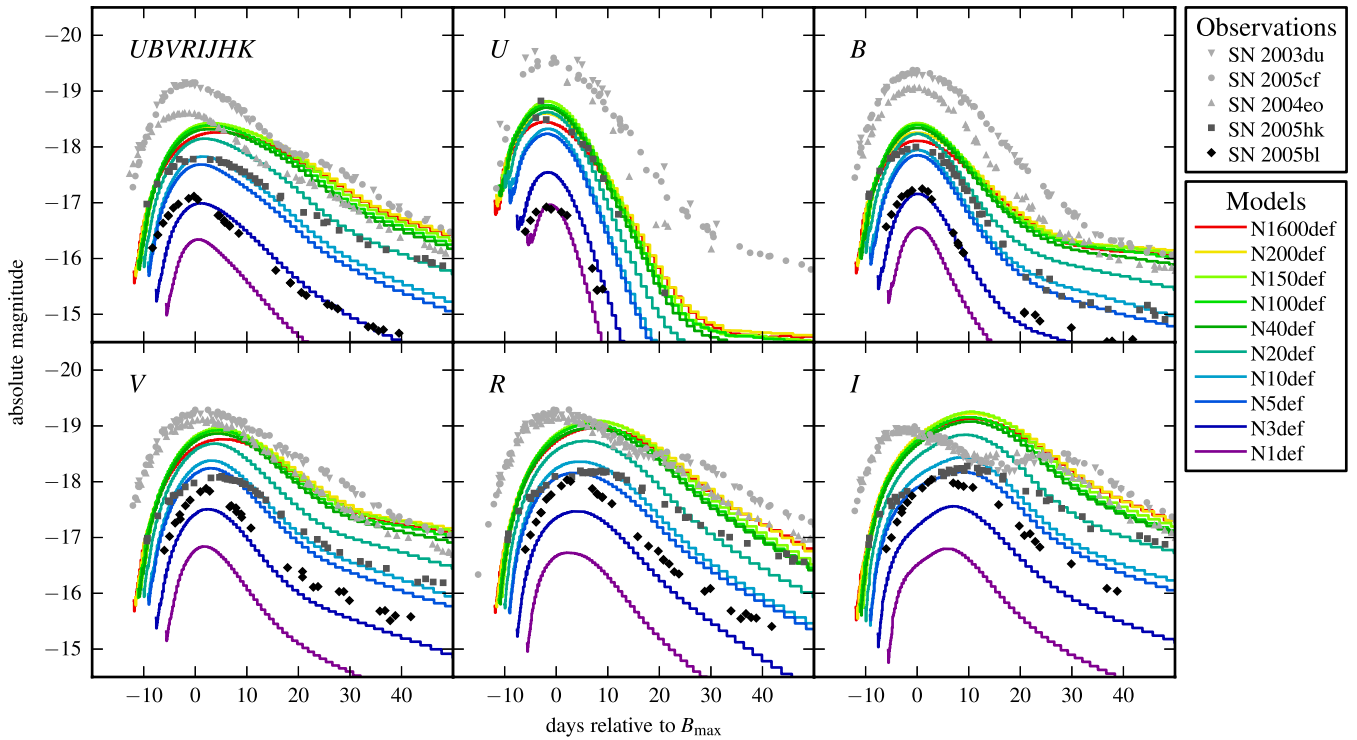
6.1 Light curves

B -band rise times (t_{max}^B), decline rate parameters (Δm_{15}^B) and peak absolute magnitudes of our angle-averaged light curves for the full model sample are given in Table 4.

Angle-averaged bolometric and broad-band light curves for select standard models are shown in Fig. 12 and compared to a set of observed SNe Ia. As discussed in detail by Kromer et al. (2013), model N5def, which leaves behind a bound remnant of $1.03 M_{\odot}$,

Table 4. Angle-averaged light curve time-scales (in days) and peak optical magnitudes for our models.

Model	t_{\max}^B	Δm_{15}^B	M_{\max}^U	M_{\max}^B	M_{\max}^V	M_{\max}^R	M_{\max}^I
N1def	7.6	2.15	-16.96	-16.55	-16.84	-16.73	-16.80
N3def	9.6	1.91	-17.55	-17.16	-17.52	-17.48	-17.53
N5def	11.1	1.69	-18.25	-17.85	-18.24	-18.16	-18.17
N10def	11.1	1.68	-18.33	-17.95	-18.38	-18.36	-18.42
N20def	12.0	1.56	-18.64	-18.24	-18.68	-18.73	-18.84
N40def	12.9	1.30	-18.70	-18.34	-18.86	-18.96	-19.08
N100Ldef	13.8	1.22	-18.80	-18.39	-18.77	-18.80	-18.92
N100def	13.1	1.31	-18.75	-18.40	-18.92	-19.03	-19.16
N100Hdef	11.5	1.44	-18.69	-18.34	-18.89	-18.99	-19.12
N150def	12.5	1.28	-18.81	-18.43	-18.96	-19.10	-19.25
N200def	13.8	1.04	-18.59	-18.26	-18.89	-19.07	-19.22
N300Cdef	12.0	1.24	-18.64	-18.25	-18.79	-18.97	-19.14
N1600def	14.0	0.95	-18.44	-18.11	-18.76	-18.97	-19.13
N1600Cdef	14.4	0.94	-18.36	-18.02	-18.62	-18.86	-19.03

**Figure 12.** Angle-averaged synthetic light curves for select models of our sample (colour coded). For comparison, light curves of several well-observed SNe Ia are overplotted as black/grey symbols: SN 2003du, 2004eo and 2005cf (Stanishev et al. 2007; Pastorello et al. 2007a,b, respectively) representing normal SNe Ia, SN 2005hk (Phillips et al. 2007) representing 2002cx-like SNe and SN 2005bl (Taubenberger et al. 2008) as a proxy for 1991bg-like SNe.

reproduces the observed light curves of SN 2005hk (Phillips et al. 2007), a prototypical event of the class of faint SNe similar to SN 2002cx (Li et al. 2003; Jha et al. 2006), remarkably well. Model N10def, which leaves behind a bound remnant of $0.926 M_{\odot}$, yields light curves fairly similar to N5def, indicating a restricted range of ignition conditions similar to those of N5def and N10def for objects like SN 2005hk or SN 2002cx.

In contrast, models with a more vigorous ignition than N10def (i.e. with $N_k \geq 20$) are not a good match to SN 2005hk: though only slightly brighter than SN 2005hk in B band, their peak magnitudes in the redder bands are significantly too bright compared to SN 2005hk: the peak magnitudes in R and I reach values typical of normal SNe Ia. However, the singly peaked R - and I -band light

curves of these models and their red $B - V$ colours at maximum light are inconsistent with observations of normal SNe Ia. Since these models would be sufficiently bright to be detected easily, the absence of any such objects in the observed transient sample could indicate that such vigorously ignited deflagrations are not realized in nature. Alternatively, it could also indicate that in this case the flame is more likely to undergo a DDT. For the evolution of our model sample assuming a DDT during the flame evolution, see S13 and Sim et al. (2013).

Models N1def and N3def are significantly fainter than SN 2005hk. N3def provides a decent match to the subluminous 1991bg-like SNe (Filippenko et al. 1992; Leibundgut et al. 1993) in bolometric and B -band light curves [see comparison to the

1991bg-like SN 2005bl (Taubenberger et al. 2008) in Fig. 12]. However, N3def cannot explain the red colours typical for those subluminescent events (the model is too bright in *U* band and too faint in *V*-, *R*- and *I*-band light curves compared to SN 2005bl). Instead, the colours and spectral properties (see next section) of models N1def and N3def are qualitatively similar to those of the brighter model N5def. Thus, N1def and N3def are promising candidates to explain some of the fainter members of the class of SN 2002cx-like SNe (or SNe Iax as recently introduced by Foley et al. 2013), which currently consists of 25 objects.

However, even N1def ($M_{\text{max}}^V = -16.84$ mag) is significantly brighter than SN 2008ha ($M_{\text{max}}^V = -14.19$ mag) the faintest object proposed to be a member of the class (Foley et al. 2009, 2013). From our present model sample it seems impossible to explain objects like SN 2008ha as the result of deflagrations in Chandrasekhar-mass WDs. Given the good agreement of N5def with SN 2005hk this could indicate that different explosion mechanisms are at work for different types of SNe Iax. However, we have not explored all possible ignition configurations yet. In particular, we have neither varied the degree of off-set of a single ignition spot from the centre in our model sample, nor the chemical composition of the initial WD. This will be the subject of a future dedicated study.

Note, however, that at least two of the SNe presented in Foley et al. (2013) showed helium lines in their spectra. This would be difficult to explain in the canonical Chandrasekhar-mass single-degenerate scenario, where a WD accretes hydrogen-rich matter from a slightly evolved main-sequence or a red giant star. However, it is possible that a CO WD may reach the Chandrasekhar mass by accretion from a helium-burning star (Iben et al. 1987; Ruiter et al. 2011; Wang & Han 2012), in which case one may expect to observe helium lines in the spectra (but, most of the helium will stably be burnt to carbon). On the other hand, more than one explosion mechanism might be at work for SNe Iax. Foley et al. (2009, 2010), for example, suggested deflagrations of helium-accreting sub-Chandrasekhar-mass WDs, while Valenti et al. (2009) and Moriya et al. (2010) favoured a core-collapse origin.

6.2 Spectra

Fig. 13 shows angle-averaged synthetic spectra for select models that cover the full distribution of ejecta and ^{56}Ni masses of our simulations and are thus representative of the full sample. Specifically, we focus on models N1def, N5def, N20def and N150def spanning a range of $0.08\text{--}1.4 M_{\odot}$ in ejecta mass and $0.03\text{--}0.38 M_{\odot}$ in ^{56}Ni mass (cf. Table 1).

Apart from differences in the absolute flux level, due to the increasing ^{56}Ni mass for more vigorously ignited models, the spectral shape along our model sequence is remarkably similar. One systematic difference is the increasing blueshift and broadening of line features that reflects the increasing ejecta velocities along the model sequence with increasing strength of the deflagration.

None of the deflagration models of our sample can account for the observed spectra of normal SNe Ia (e.g. SN 2005cf) since neither the spectral features nor the absolute flux distribution match. In particular, our early time model spectra lack the strong absorption features, associated with atomic lines of IMEs, such as Si, S and Ca, that are characteristic of normal SNe Ia.

Instead, the spectral features of our deflagration models provide a good match to 2002cx-like SNe. As discussed by Kromer et al. (2013), in particular model N5def nicely reproduces the overall flux level and spectral features of SN 2005hk, a prototypical 2002cx-like event. Comparably good agreement is found for model N10def. The

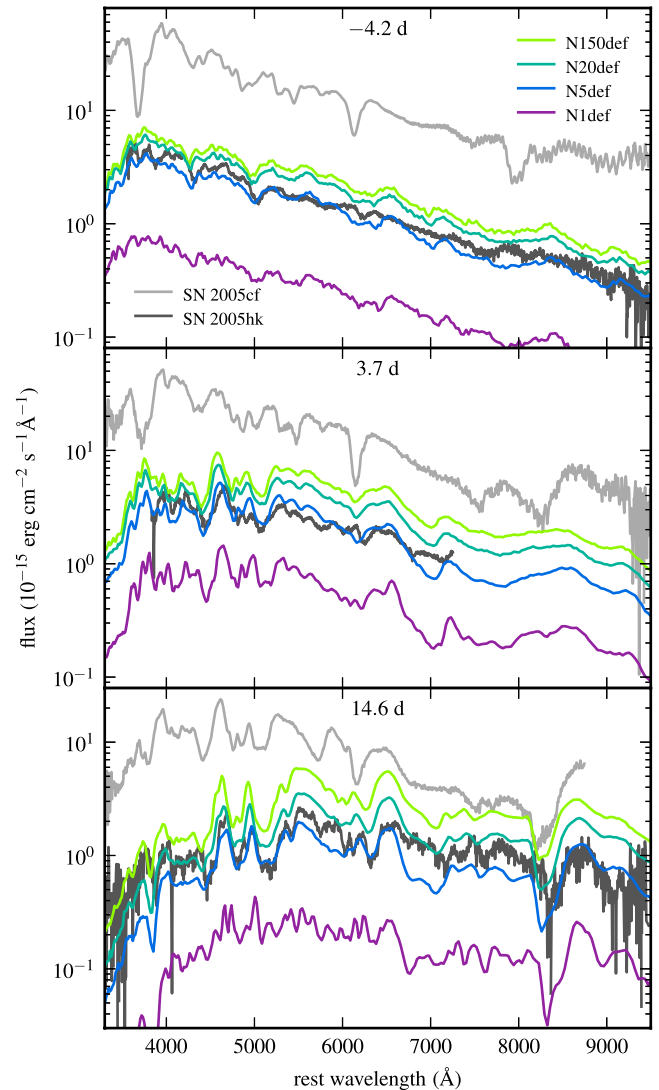


Figure 13. Spectral evolution for select models (colour coded) of our sample. Shown are snapshots for -4.2 , 3.7 and 14.6 d relative to *B*-band maximum (from top to bottom; see Table 4 for the rise times of the different models). For comparison, observed spectra of SN 2005hk (dark grey; Phillips et al. 2007) and SN 2005cf (grey; Garavini et al. 2007) are over-plotted for corresponding epochs. The observations were de-reddened and de-redshifted.

more vigorously ignited models such as N20def and N150def are too bright compared to SN 2005hk, while the flux for models with a weaker deflagration (e.g. N1def) is too low.

6.3 Viewing-angle dependence

In the previous sections, we have discussed angle-averaged light curves and spectra of our deflagration models. However, since our models show (more or less pronounced) large-scale asymmetries (see Section 5.3), the synthetic observables depend on the viewing angle of the observer. This is taken into account by our 3D radiative transfer code ARTIS.

Fig. 14 shows line-of-sight dependent synthetic light curves for four models (N1def, N5def, N20def and N150def) that cover the full distribution of ejecta and ^{56}Ni masses predicted by our set of simulations. As for other explosion models (see e.g. Kromer &

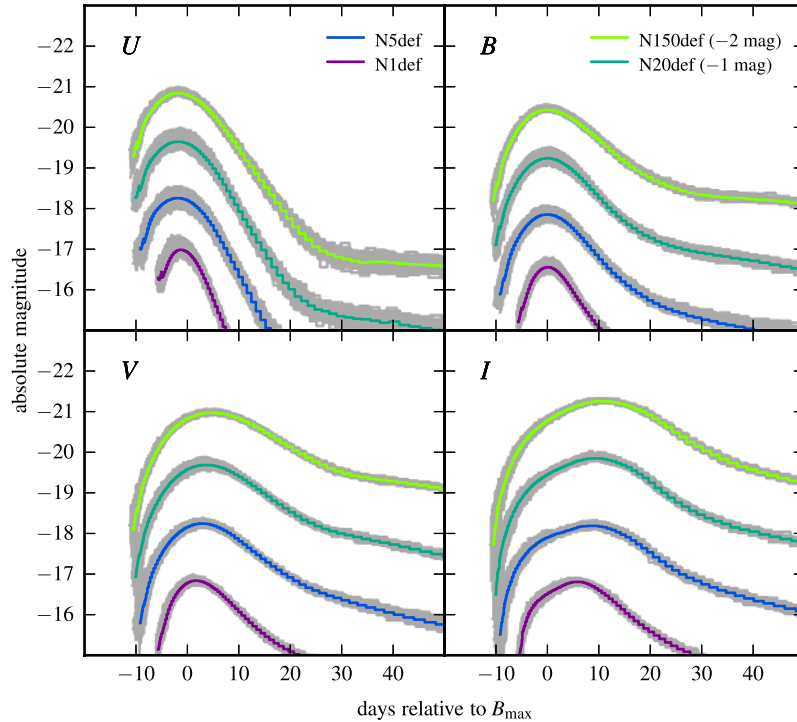


Figure 14. Synthetic light curves as seen from 100 different viewing angles (each of equal solid angle) for select models of our sample in grey. The coloured lines show the angle-averaged light curves for comparison. For clarity, the light curves of models N20def and N150def are shifted by -1 and -2 mag, respectively.

Sim 2009; Kromer et al. 2010; Röpke et al. 2012), the line-of-sight dependence weakens from blue to red bands since the optical depth decreases with wavelength.

As discussed in Section 5.3, weak deflagrations (N1def, N5def and N20def) tend to evolve in a one-sided manner and preserve parts of this asymmetry into the homologous expansion phase. Thus, these models tend to show a slightly stronger viewing-angle sensitivity than vigorously ignited models with intermediate N_k , such as N150def, that evolve in a very symmetric way and show little large-scale asymmetry. In general, however, the viewing-angle dependence in all of our models is moderate.

7 SUMMARY

To study the question of whether pure deflagrations of Chandrasekhar-mass WDs in the single-degenerate scenario contribute to the observed sample of SNe Ia, we have carried out an extensive study of explosion models. This work presents 3D full-star hydrodynamic simulations for a wide range of explosion strengths, combined with detailed nucleosynthesis and 3D radiative transfer calculations that provide synthetic observables, which can be *directly* compared to observations. This goes beyond previous studies of model sequences, which assess the validity of the pure deflagration explosion mechanism based only on holistic, qualitative arguments.

The major result of the hydrodynamic simulations is the occurrence of a bound remnant in sparsely ignited deflagrations ($N_k \lesssim 100$) with an energy release $E_{\text{nuc}} \lesssim 1.1 \times 10^{51}$ erg (cf. Jordan et al. 2012b). The remnant is mostly comprised of the unburnt matter that remains in the centre of the star. Most of the hot deflagration ashes are ejected and reach homologous expansion. We find a roughly linear relation between the ejecta mass (and also

the ^{56}Ni mass) and E_{nuc} (see Fig. 7). The remnant masses in our sample lie between 1.32 and $0.09 M_{\odot}$ and the ejected ^{56}Ni masses are in the range 0.035 – $0.38 M_{\odot}$. Pulsations in the bound material were found to not re-ignite explosive burning above a certain deflagration strength (for $N_k \geq 5$). However, for our two weakest deflagrations (N1def and N3def), re-ignition of the remnant could not be excluded.

The bound remnants are enriched (mainly in the outer layers) with 3–10 per cent of IGE- and IME-rich deflagration ashes that were not accelerated to escape velocity. In our simulations performed on a grid co-expanding with the ejecta, we find kick velocities of the remnants of the order of $v_{\text{kick}} \leq 36 \text{ km s}^{-1}$ (both with our monopole gravity solver as well as in two tests with a fast Fourier transformation-based gravity solver). Such low kick velocities are contrary to the recent results of Jordan et al. (2012b) and may be insufficient for the ejection of the remnant objects from the binary systems.

As the explosion energies of our models are low, the same is true also for the maximum ejecta velocities, which lie in the range 9000 – $14\,000 \text{ km s}^{-1}$. The ejecta show the complex structures typical for deflagrations and both ^{56}Ni and unburnt C/O material can be found at all ejecta velocities. Interestingly, the fraction of the ejecta comprised of burnt material increases with decreasing deflagration strength.

According to our synthetic colour light curves and spectra, the two relatively sparsely ignited models N5def and N10def (which leave bound remnants) are promising candidates for 2002cx-like SNe. More vigorously ignited models are neither comparable to 2002cx-like SNe (too bright at red wavelengths), nor to normal SNe Ia (R - and I -band light curves are only singly peaked, $B - V$ colours at maximum light disagree and the model spectra lack strong lines of IMEs such as Si, S and Ca). More sparsely ignited models

may be interesting candidates for some of the fainter members of 2002cx-like SNe. But, the faintest observed events (like SN 2008ha) of the Foley et al. (2013) SN Iax seem to be out of reach for our current set of models.

A restricted range of sparse one-sided ignition configurations (N5def, N10def) with an energy release $E_{\text{nuc}} \sim 0.5 \times 10^{51}$ erg leads to models that account for the observed properties of SN 2002cx-like events. Although we initiate our deflagrations in the multiple ignition spot parametrization, this range of ignition conditions bears some similarity with the findings of recent pre-ignition simulations (Nonaka et al. 2012) that predict off-centre ignition in a single bubble at a radial distance in the range 40–75 km. We find that more vigorously ignited deflagrations ($N_k \gtrsim 20$) do not resemble any observed class of SN Ia. This could either mean that such ignition conditions are not realized in nature. Alternatively, perhaps strong deflagrations always trigger a DDT, leading to brighter events: our DDT models with $N_k \sim 100$ have been shown to compare well with normal SNe Ia (Röpke et al. 2012; S13; Sim et al. 2013).

ACKNOWLEDGEMENTS

The simulations presented here were carried out in part on the JUGENE supercomputer at the Forschungszentrum Jülich within the Partnership for Advanced Computing in Europe (PRA026), the grant HMU13 and in part at the Computer Center of the Max Planck Society, Garching, Germany. This work was also supported by the Deutsche Forschungsgemeinschaft via the Transregional Collaborative Research Center TRR 33 ‘The Dark Universe’, the Emmy Noether Programme (RO 3676/1-1), the ARCHES prize of the German Ministry of Education and Research (BMBF), the graduate school ‘Theoretical Astrophysics and Particle Physics’ at the University of Würzburg (GRK 1147) and the Excellence Cluster EXC 153. MF, FKR and SAS acknowledge travel support by the DAAD/Go8 German–Australian exchange programme. RP acknowledges support by the European Research Council (ERC-StG grant EXAGAL-308037).

REFERENCES

- Blinnikov S. I., Khokhlov A. M., 1986, *Sov. Astron. Lett.*, 12, 131
 Blinnikov S. I., Khokhlov A. M., 1987, *Sov. Astron. Lett.*, 13, 364
 Branch D., Baron E., Thomas R. C., Kasen D., Li W., Filippenko A. V., 2004, *PASP*, 116, 903
 Bravo E., García-Senz D., 2009, *ApJ*, 695, 1244
 Ciaraldi-Schoolmann F., Seitenzahl I. R., Röpke F. K., 2013, *A&A*, 559, A117
 Dilday B. et al., 2012, *Science*, 337, 942
 Filippenko A. V. et al., 1992, *AJ*, 104, 1543
 Fink M., Röpke F. K., Hillebrandt W., Seitenzahl I. R., Sim S. A., Kromer M., 2010, *A&A*, 514, A53
 Foley R. J. et al., 2009, *AJ*, 138, 376
 Foley R. J., Brown P. J., Rest A., Challis P. J., Kirshner R. P., Wood-Vasey W. M., 2010, *ApJ*, 708, L61
 Foley R. J. et al., 2013, *ApJ*, 767, 57
 Gamezo V. N., Khokhlov A. M., Oran E. S., Chtchelkanova A. Y., Rosenberg R. O., 2003, *Science*, 299, 77
 Garavini G. et al., 2007, *A&A*, 471, 527
 García-Senz D., Bravo E., 2005, *A&A*, 430, 585
 Hillebrandt W., Niemeyer J. C., 2000, *ARA&A*, 38, 191
 Hillebrandt W., Kromer M., Röpke F. K., Ruiter A. J., 2013, *Frontiers Phys.*, 8, 116
 Iben I., Jr, Nomoto K., Tornambe A., Tutukov A. V., 1987, *ApJ*, 317, 717
 Jha S., Branch D., Chornock R., Foley R. J., Li W., Swift B. J., Casebeer D., Filippenko A. V., 2006, *AJ*, 132, 189
 Jordan G. C., IV et al., 2012a, *ApJ*, 759, 53
 Jordan G. C., IV, Perets H. B., Fisher R. T., van Rossum D. R., 2012b, *ApJ*, 761, L23
 Kasen D., Röpke F. K., Woosley S. E., 2009, *Nature*, 460, 869
 Khokhlov A. M., 1991, *A&A*, 245, 114
 Kromer M., Sim S. A., 2009, *MNRAS*, 398, 1809
 Kromer M., Sim S. A., Fink M., Röpke F. K., Seitenzahl I. R., Hillebrandt W., 2010, *ApJ*, 719, 1067
 Kromer M. et al., 2013, *MNRAS*, 429, 2287
 Leibundgut B. et al., 1993, *AJ*, 105, 301
 Li W. et al., 2003, *PASP*, 115, 453
 Long M. et al., 2013, preprint ([arXiv:1307.8221](https://arxiv.org/abs/1307.8221))
 Ma H., Woosley S. E., Malone C. M., Almgren A., Bell J., 2013, *ApJ*, 771, 58
 Moll R., Woosley S. E., 2013, *ApJ*, 774, 137
 Moriya T., Tominaga N., Tanaka M., Nomoto K., Sauer D. N., Mazzali P. A., Maeda K., Suzuki T., 2010, *ApJ*, 719, 1445
 Niemeyer J. C., 1999, *ApJ*, 523, L57
 Nonaka A., Aspden A. J., Zingale M., Almgren A. S., Bell J. B., Woosley S. E., 2012, *ApJ*, 745, 73
 Osher S., Sethian J. A., 1988, *J. Comput. Phys.*, 79, 12
 Pakmor R., Kromer M., Taubenberger S., Springel V., 2013, *ApJ*, 770, L8
 Parikh A., José J., Seitenzahl I. R., Röpke F. K., 2013, *A&A*, 557, A3
 Pastorello A. et al., 2007a, *MNRAS*, 377, 1531
 Pastorello A. et al., 2007b, *MNRAS*, 376, 1301
 Patat F. et al., 2007, *Science*, 317, 924
 Phillips M. M. et al., 2007, *PASP*, 119, 360
 Plewa T., Calder A. C., Lamb D. Q., 2004, *ApJ*, 612, L37
 Rauscher T., Thielemann F. K., 2000, *At. Data Nucl. Data Tables*, 75, 1
 Reinecke M., Hillebrandt W., Niemeyer J. C., Klein R., Gröbl A., 1999, *A&A*, 347, 724
 Reinecke M., Hillebrandt W., Niemeyer J. C., 2002a, *A&A*, 386, 936
 Reinecke M., Hillebrandt W., Niemeyer J. C., 2002b, *A&A*, 391, 1167
 Röpke F. K., 2005, *A&A*, 432, 969
 Röpke F. K., Gieseler M., Reinecke M., Travaglio C., Hillebrandt W., 2006a, *A&A*, 453, 203
 Röpke F. K., Hillebrandt W., Niemeyer J. C., Woosley S. E., 2006b, *A&A*, 448, 1
 Röpke F. K., Woosley S. E., Hillebrandt W., 2007a, *ApJ*, 660, 1344
 Röpke F. K., Hillebrandt W., Schmidt W., Niemeyer J. C., Blinnikov S. I., Mazzali P. A., 2007b, *ApJ*, 668, 1132
 Röpke F. K. et al., 2012, *ApJ*, 750, L19
 Ruiter A. J., Belczynski K., Sim S. A., Hillebrandt W., Fryer C. L., Fink M., Kromer M., 2011, *MNRAS*, 417, 408
 Ruiter A. J. et al., 2013, *MNRAS*, 429, 1425
 Schmidt W., Niemeyer J. C., Hillebrandt W., 2006a, *A&A*, 450, 265
 Schmidt W., Niemeyer J. C., Hillebrandt W., Röpke F. K., 2006b, *A&A*, 450, 283
 Seitenzahl I. R., Meakin C. A., Townsley D. M., Lamb D. Q., Truran J. W., 2009a, *ApJ*, 696, 515
 Seitenzahl I. R., Meakin C. A., Lamb D. Q., Truran J. W., 2009b, *ApJ*, 700, 642
 Seitenzahl I. R., Townsley D. M., Peng F., Truran J. W., 2009c, *At. Data Nucl. Data Tables*, 95, 96
 Seitenzahl I. R., Röpke F. K., Fink M., Pakmor R., 2010, *MNRAS*, 407, 2297
 Seitenzahl I. R., Ciaraldi-Schoolmann F., Röpke F. K., 2011, *MNRAS*, 414, 2709
 Seitenzahl I. R. et al., 2013, *MNRAS*, 429, 1156 (S13)
 Shen K. J., Guillochon J., Foley R. J., 2013, *ApJ*, 770, L35
 Sim S. A., 2007, *MNRAS*, 375, 154
 Sim S. A. et al., 2013, *MNRAS*, 436, 333
 Smiljanovski V., Moser V., Klein R., 1997, *Combust. Theory Modelling*, 1, 183
 Soker N., Kashi A., García-Berro E., Torres S., Camacho J., 2013, *MNRAS*, 431, 1541
 Stanishev V. et al., 2007, *A&A*, 469, 645
 Stehle M., Mazzali P. A., Benetti S., Hillebrandt W., 2005, *MNRAS*, 360, 1231

Sternberg A. et al., 2011, *Science*, 333, 856
 Stritzinger M., Leibundgut B., Walch S., Contardo G., 2006, *A&A*, 450, 241
 Taubenberger S. et al., 2008, *MNRAS*, 385, 75
 Travaglio C., Hillebrandt W., Reinecke M., Thielemann F. K., 2004, *A&A*, 425, 1029
 Travaglio C., Röpke F. K., Gallino R., Hillebrandt W., 2011, *ApJ*, 739, 93
 Valenti S. et al., 2009, *Nature*, 459, 674
 Wang B., Han Z., 2012, *New Astron. Rev.*, 56, 122
 Woosley S. E., Kasen D., 2011, *ApJ*, 734, 38

APPENDIX A: DEFLAGRATION TABLES

To calibrate the energy release in the deflagration, we have used an iterative scheme in which we alternate between a sample hydrodynamic explosion simulation and detailed nucleosynthesis post-processing calculations, as described in the appendix of Fink et al. (2010). We have tabulated the final composition of deflagration ashes in CO matter for our reduced set of species (see Section 3.1)

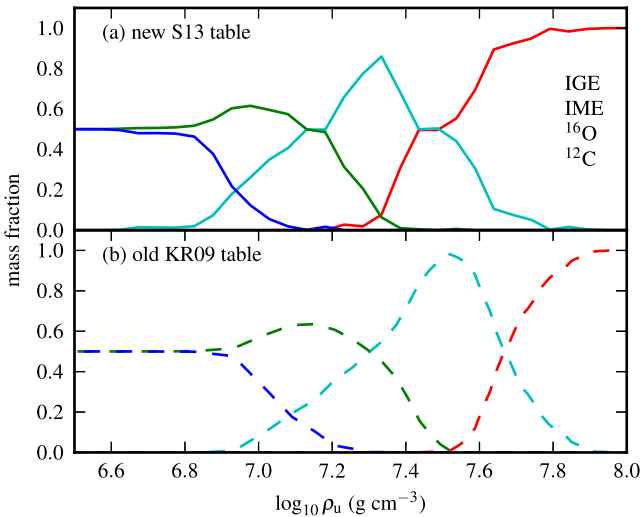


Figure A1. Mass fractions of the reduced species in our CO deflagration tables against the density of the unburnt fuel ρ_u .

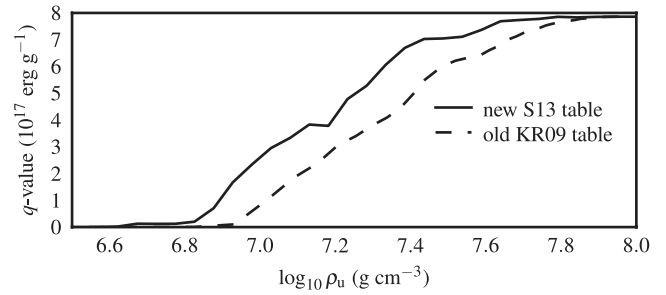


Figure A2. Reaction q -values against ρ_u for our CO deflagration tables.

as a function of the density in the unburnt matter, ρ_u . In contrast to previous studies, in which we used our old KR09 deflagration table (Kasen, Röpke & Woosley 2009; Seitenzahl et al. 2010; Seitenzahl, Ciaraldi-Schoolmann & Röpke 2011; Travaglio et al. 2011; Ciaraldi-Schoolmann, Seitenzahl & Röpke 2013; Parikh et al. 2013; see Fig. A1b), here, we use an improved algorithm to determine the value of ρ_u in ‘mixed’ cells intersected by the flame (the old algorithm overestimated ρ_u in some cases). Our new S13 deflagration table is shown in Fig. A1(a) and is used in this study and in Seitenzahl et al. (2013). The differences between the old and the new table are moderate: as shown in Fig. A2, the reaction q -value curve is shifted somewhat towards lower fuel densities ρ_u . With the new table, the consistency between the nuclear energy release in our hydrodynamic simulations and our detailed post-processing nucleosynthesis results is improved.

APPENDIX B: DETAILED NUCLEOSYNTHETIC YIELDS

Total integrated nucleosynthetic yields of stable and radioactive nuclei in the model ejecta are given in Tables B1 and B2. Tables B3 and B4 provide the respective data for the remnant objects. For radioactive nuclei, we simply tabulate the values at the end of our post-processing calculation ($t = 100$ s). To determine the yields of stable nuclei, we decay all radioactive nuclei with half-lives of less than 2 Gyr. Yields of radioactive nuclei with longer half-lives are given with their $t = 100$ s value among the stable isotopes.

Table B1. Asymptotic yields of stable isotopes in the model ejecta in solar masses.

	N1def	N3def	N5def	N10def	N20def	N40def	N100Ldef	N100def	N100Hdef	N150def	N200def	N300Cdef	N1600def	N1600Cdef
M_{totEj}	8.43×10^{-2}	1.95×10^{-1}	3.72×10^{-1}	4.78×10^{-1}	8.59×10^{-1}	$1.21 \times 10^{+0}$	$1.23 \times 10^{+0}$	$1.31 \times 10^{+0}$	$1.31 \times 10^{+0}$	$1.40 \times 10^{+0}$	$1.40 \times 10^{+0}$	$1.40 \times 10^{+0}$	$1.40 \times 10^{+0}$	$1.40 \times 10^{+0}$
${}^4\text{He}$	5.18×10^{-5}	7.82×10^{-5}	1.10×10^{-4}	1.29×10^{-4}	1.62×10^{-4}	2.02×10^{-4}	2.41×10^{-4}	2.15×10^{-4}	1.90×10^{-4}	2.43×10^{-4}	1.92×10^{-4}	1.95×10^{-4}	1.76×10^{-4}	1.79×10^{-4}
${}^{12}\text{C}$	1.15×10^{-2}	2.38×10^{-2}	4.31×10^{-2}	5.99×10^{-2}	1.26×10^{-1}	2.17×10^{-1}	2.87×10^{-1}	2.47×10^{-1}	1.84×10^{-1}	2.60×10^{-1}	2.71×10^{-1}	2.86×10^{-1}	2.89×10^{-1}	3.10×10^{-1}
${}^{13}\text{C}$	8.75×10^{-9}	2.48×10^{-8}	3.06×10^{-8}	4.51×10^{-8}	3.47×10^{-7}	1.73×10^{-6}	1.80×10^{-7}	2.16×10^{-6}	7.26×10^{-7}	2.39×10^{-6}	1.00×10^{-6}	1.58×10^{-6}	1.11×10^{-6}	5.28×10^{-7}
${}^{14}\text{N}$	1.63×10^{-6}	5.15×10^{-6}	6.37×10^{-6}	9.46×10^{-6}	3.31×10^{-5}	6.09×10^{-5}	3.52×10^{-5}	7.33×10^{-5}	6.49×10^{-5}	7.04×10^{-5}	5.35×10^{-5}	7.61×10^{-5}	4.90×10^{-5}	3.79×10^{-5}
${}^{15}\text{N}$	2.31×10^{-9}	7.82×10^{-9}	9.52×10^{-9}	1.45×10^{-8}	6.25×10^{-8}	1.34×10^{-7}	5.41×10^{-8}	4.77×10^{-7}	1.55×10^{-7}	1.30×10^{-7}	8.89×10^{-8}	1.37×10^{-7}	7.68×10^{-8}	5.75×10^{-8}
${}^{16}\text{O}$	1.57×10^{-2}	3.57×10^{-2}	5.99×10^{-2}	8.50×10^{-2}	1.89×10^{-1}	3.03×10^{-1}	3.66×10^{-1}	3.34×10^{-1}	3.07×10^{-1}	3.54×10^{-1}	3.53×10^{-1}	3.81×10^{-1}	3.66×10^{-1}	3.90×10^{-1}
${}^{17}\text{O}$	2.39×10^{-7}	7.19×10^{-7}	9.03×10^{-7}	1.32×10^{-6}	4.35×10^{-6}	7.64×10^{-6}	4.97×10^{-6}	9.24×10^{-6}	8.33×10^{-6}	9.64×10^{-6}	7.82×10^{-6}	1.07×10^{-5}	8.02×10^{-6}	5.70×10^{-6}
${}^{18}\text{O}$	3.15×10^{-9}	1.14×10^{-8}	1.35×10^{-8}	2.12×10^{-8}	1.22×10^{-7}	3.05×10^{-7}	8.23×10^{-8}	3.54×10^{-7}	3.28×10^{-7}	2.88×10^{-7}	1.78×10^{-7}	2.99×10^{-7}	1.40×10^{-7}	8.83×10^{-8}
${}^{19}\text{F}$	2.81×10^{-11}	9.97×10^{-11}	1.23×10^{-10}	1.93×10^{-10}	1.07×10^{-9}	2.72×10^{-9}	7.07×10^{-9}	2.84×10^{-9}	3.16×10^{-9}	2.30×10^{-9}	1.37×10^{-9}	2.31×10^{-9}	1.08×10^{-9}	7.48×10^{-10}
${}^{20}\text{Ne}$	7.62×10^{-4}	2.38×10^{-3}	3.05×10^{-3}	5.09×10^{-3}	1.95×10^{-2}	3.10×10^{-2}	1.56×10^{-2}	2.67×10^{-2}	6.26×10^{-2}	2.60×10^{-2}	1.85×10^{-2}	2.52×10^{-2}	1.61×10^{-2}	1.58×10^{-2}
${}^{21}\text{Ne}$	1.73×10^{-7}	5.66×10^{-7}	7.16×10^{-7}	1.09×10^{-6}	4.99×10^{-6}	1.08×10^{-5}	3.95×10^{-6}	1.23×10^{-5}	1.20×10^{-5}	1.06×10^{-5}	6.89×10^{-6}	1.08×10^{-5}	5.64×10^{-6}	4.18×10^{-6}
${}^{22}\text{Ne}$	5.75×10^{-4}	1.17×10^{-3}	2.15×10^{-3}	2.98×10^{-3}	6.01×10^{-3}	1.03×10^{-2}	1.45×10^{-2}	1.17×10^{-2}	8.47×10^{-3}	1.25×10^{-2}	1.34×10^{-2}	1.39×10^{-2}	1.45×10^{-2}	1.57×10^{-2}
${}^{23}\text{Na}$	1.27×10^{-5}	4.00×10^{-5}	5.06×10^{-5}	8.05×10^{-5}	3.63×10^{-4}	7.58×10^{-4}	2.79×10^{-4}	7.69×10^{-4}	1.06×10^{-3}	6.78×10^{-4}	4.40×10^{-4}	6.75×10^{-4}	3.78×10^{-4}	2.95×10^{-4}
${}^{24}\text{Mg}$	9.79×10^{-4}	2.98×10^{-3}	3.94×10^{-3}	6.09×10^{-3}	1.63×10^{-2}	2.10×10^{-2}	1.81×10^{-2}	2.06×10^{-2}	3.23×10^{-2}	2.27×10^{-2}	1.92×10^{-2}	2.27×10^{-2}	1.76×10^{-2}	1.82×10^{-2}
${}^{25}\text{Mg}$	1.69×10^{-5}	5.32×10^{-5}	6.80×10^{-5}	1.06×10^{-4}	4.26×10^{-4}	8.06×10^{-4}	3.60×10^{-4}	8.28×10^{-4}	1.14×10^{-3}	7.50×10^{-4}	5.17×10^{-4}	7.63×10^{-4}	4.45×10^{-4}	3.75×10^{-4}
${}^{26}\text{Mg}$	2.43×10^{-5}	7.34×10^{-5}	9.62×10^{-5}	1.51×10^{-4}	5.86×10^{-4}	1.06×10^{-3}	5.06×10^{-3}	1.01×10^{-3}	1.69×10^{-3}	9.26×10^{-4}	6.44×10^{-4}	9.23×10^{-4}	5.51×10^{-4}	5.16×10^{-4}
${}^{27}\text{Al}$	6.42×10^{-3}	1.51×10^{-2}	2.48×10^{-2}	4.22×10^{-2}	1.43×10^{-1}	2.13×10^{-1}	1.27×10^{-1}	1.88×10^{-1}	4.05×10^{-1}	1.89×10^{-1}	1.42×10^{-1}	1.85×10^{-1}	1.26×10^{-1}	1.27×10^{-1}
${}^{28}\text{Si}$	5.24×10^{-3}	1.51×10^{-2}	2.48×10^{-2}	3.45×10^{-2}	7.23×10^{-2}	7.97×10^{-2}	8.04×10^{-2}	8.39×10^{-2}	9.45×10^{-2}	9.43×10^{-2}	8.46×10^{-2}	9.62×10^{-2}	7.63×10^{-2}	7.89×10^{-2}
${}^{29}\text{Si}$	5.88×10^{-5}	1.72×10^{-4}	2.34×10^{-4}	3.55×10^{-4}	9.29×10^{-4}	1.21×10^{-3}	1.06×10^{-3}	1.19×10^{-3}	1.76×10^{-3}	1.33×10^{-3}	1.13×10^{-3}	1.33×10^{-3}	1.04×10^{-3}	1.07×10^{-3}
${}^{30}\text{Si}$	1.09×10^{-4}	3.18×10^{-4}	4.33×10^{-4}	6.51×10^{-4}	1.57×10^{-3}	1.94×10^{-3}	1.92×10^{-3}	2.01×10^{-3}	2.55×10^{-3}	2.26×10^{-3}	1.98×10^{-3}	2.28×10^{-3}	1.84×10^{-3}	1.92×10^{-3}
${}^{31}\text{P}$	2.53×10^{-5}	7.67×10^{-5}	1.03×10^{-4}	1.57×10^{-4}	3.93×10^{-4}	4.73×10^{-4}	4.49×10^{-4}	4.80×10^{-4}	6.50×10^{-4}	5.44×10^{-4}	4.76×10^{-4}	5.48×10^{-4}	4.36×10^{-4}	4.52×10^{-4}
${}^{32}\text{S}$	1.77×10^{-3}	4.99×10^{-3}	8.59×10^{-3}	1.16×10^{-2}	2.30×10^{-2}	2.51×10^{-2}	2.54×10^{-2}	2.65×10^{-2}	2.99×10^{-2}	2.97×10^{-2}	2.68×10^{-2}	3.02×10^{-2}	2.40×10^{-2}	2.50×10^{-2}
${}^{33}\text{S}$	8.11×10^{-6}	2.38×10^{-5}	3.52×10^{-5}	5.07×10^{-5}	1.15×10^{-4}	1.28×10^{-4}	1.27×10^{-4}	1.35×10^{-4}	1.49×10^{-4}	1.52×10^{-4}	1.36×10^{-4}	1.54×10^{-4}	1.24×10^{-4}	1.28×10^{-4}
${}^{34}\text{S}$	8.17×10^{-5}	2.34×10^{-4}	3.68×10^{-4}	5.24×10^{-4}	1.17×10^{-3}	1.29×10^{-3}	1.32×10^{-3}	1.37×10^{-3}	1.47×10^{-3}	1.54×10^{-3}	1.38×10^{-3}	1.58×10^{-3}	1.26×10^{-3}	1.30×10^{-3}
${}^{36}\text{S}$	1.11×10^{-8}	3.03×10^{-8}	4.14×10^{-8}	6.04×10^{-8}	1.31×10^{-7}	1.67×10^{-7}	1.78×10^{-7}	1.79×10^{-7}	1.81×10^{-7}	2.03×10^{-7}	1.82×10^{-7}	2.01×10^{-7}	1.71×10^{-7}	1.81×10^{-7}
${}^{35}\text{Cl}$	4.96×10^{-6}	1.49×10^{-5}	2.08×10^{-5}	3.05×10^{-5}	7.07×10^{-5}	7.94×10^{-5}	7.83×10^{-5}	8.31×10^{-5}	9.29×10^{-5}	9.45×10^{-5}	8.41×10^{-5}	9.48×10^{-5}	7.63×10^{-5}	7.95×10^{-5}
${}^{37}\text{Cl}$	5.91×10^{-7}	1.75×10^{-6}	2.78×10^{-6}	3.87×10^{-6}	8.58×10^{-6}	9.00×10^{-6}	8.53×10^{-6}	9.36×10^{-6}	1.10×10^{-5}	1.05×10^{-5}	9.45×10^{-6}	1.08×10^{-5}	8.39×10^{-6}	8.56×10^{-6}
${}^{36}\text{Ar}$	2.71×10^{-4}	7.35×10^{-4}	1.32×10^{-3}	1.73×10^{-3}	3.25×10^{-3}	3.57×10^{-3}	3.60×10^{-3}	3.78×10^{-3}	4.30×10^{-3}	4.20×10^{-3}	3.81×10^{-3}	4.24×10^{-3}	3.40×10^{-3}	3.56×10^{-3}
${}^{38}\text{Ar}$	3.29×10^{-5}	9.81×10^{-5}	1.59×10^{-4}	2.23×10^{-4}	5.04×10^{-4}	5.32×10^{-4}	5.22×10^{-4}	5.57×10^{-4}	6.37×10^{-4}	6.27×10^{-4}	5.65×10^{-4}	6.48×10^{-4}	5.05×10^{-4}	5.16×10^{-4}
${}^{40}\text{Ar}$	2.67×10^{-10}	7.55×10^{-10}	1.02×10^{-9}	1.52×10^{-9}	3.53×10^{-9}	4.05×10^{-9}	3.94×10^{-9}	4.22×10^{-9}	4.80×10^{-9}	4.72×10^{-9}	4.18×10^{-9}	4.62×10^{-9}	3.82×10^{-9}	4.02×10^{-9}
${}^{39}\text{K}$	1.73×10^{-6}	5.20×10^{-6}	8.21×10^{-6}	1.15×10^{-5}	2.61×10^{-5}	2.67×10^{-5}	2.48×10^{-5}	2.76×10^{-5}	3.42×10^{-5}	3.10×10^{-5}	2.77×10^{-5}	3.17×10^{-5}	2.44×10^{-5}	2.49×10^{-5}
${}^{41}\text{K}$	9.08×10^{-8}	2.69×10^{-7}	4.31×10^{-7}	5.93×10^{-7}	1.32×10^{-6}	1.35×10^{-6}	1.25×10^{-6}	1.40×10^{-6}	1.73×10^{-6}	1.57×10^{-6}	1.41×10^{-6}	1.61×10^{-6}	1.24×10^{-6}	1.26×10^{-6}
${}^{40}\text{Ca}$	2.31×10^{-4}	6.12×10^{-4}	1.14×10^{-3}	1.46×10^{-3}	2.62×10^{-3}	2.92×10^{-3}	2.96×10^{-3}	3.11×10^{-3}	3.52×10^{-3}	3.43×10^{-3}	3.14×10^{-3}	3.45×10^{-3}	2.82×10^{-3}	2.96×10^{-3}
${}^{42}\text{Ca}$	6.68×10^{-7}	2.03×10^{-6}	3.25×10^{-6}	4.55×10^{-6}	1.07×10^{-5}	1.08×10^{-5}	1.00×10^{-5}	1.12×10^{-5}	1.39×10^{-5}	1.26×10^{-5}	1.13×10^{-5}	1.30×10^{-5}	9.91×10^{-6}	1.01×10^{-5}
${}^{43}\text{Ca}$	1.46×10^{-9}	3.78×10^{-9}	5.36×10^{-9}	7.83×10^{-9}	2.01×10^{-8}	1.95×10^{-8}	1.56×10^{-8}	1.88×10^{-8}	2.64×10^{-8}	2.11×10^{-8}	1.77×10^{-8}	2.04×10^{-8}	1.53×10^{-8}	1.53×10^{-8}

Table B1 – *continued*

	N1def	N3def	N5def	N10def	N20def	N40def	N100Ldef	N100def	N100Hdef	N150def	N200def	N300Cdef	N1600def	N1600Cdef
44Ca	1.97 × 10 ⁻⁷	4.83 × 10 ⁻⁷	8.98 × 10 ⁻⁷	1.12 × 10 ⁻⁶	1.90 × 10 ⁻⁶	2.16 × 10 ⁻⁶	2.07 × 10 ⁻⁶	2.30 × 10 ⁻⁶	2.58 × 10 ⁻⁶	2.52 × 10 ⁻⁶	2.33 × 10 ⁻⁶	2.46 × 10 ⁻⁶	2.10 × 10 ⁻⁶	2.15 × 10 ⁻⁶
46Ca	4.82 × 10 ⁻¹³	1.22 × 10 ⁻¹²	1.97 × 10 ⁻¹²	2.70 × 10 ⁻¹²	6.42 × 10 ⁻¹²	6.42 × 10 ⁻¹²	5.59 × 10 ⁻¹²	6.77 × 10 ⁻¹²	6.67 × 10 ⁻¹²	7.26 × 10 ⁻¹²	6.12 × 10 ⁻¹²	1.06 × 10 ⁻¹¹	5.47 × 10 ⁻¹²	5.75 × 10 ⁻¹²
48Ca	7.17 × 10 ⁻¹⁶	1.92 × 10 ⁻¹⁵	5.29 × 10 ⁻¹⁵	5.09 × 10 ⁻¹⁵	1.51 × 10 ⁻¹⁴	3.07 × 10 ⁻¹⁴	1.03 × 10 ⁻¹⁴	5.12 × 10 ⁻¹⁴	9.58 × 10 ⁻¹⁴	2.15 × 10 ⁻¹⁴	3.03 × 10 ⁻¹⁴	8.17 × 10 ⁻¹⁴	9.48 × 10 ⁻¹⁴	1.06 × 10 ⁻¹⁴
45Sc	3.03 × 10 ⁻⁹	8.45 × 10 ⁻⁹	1.40 × 10 ⁻⁸	1.89 × 10 ⁻⁸	3.88 × 10 ⁻⁸	4.05 × 10 ⁻⁸	3.50 × 10 ⁻⁸	4.15 × 10 ⁻⁸	5.35 × 10 ⁻⁸	4.61 × 10 ⁻⁸	4.17 × 10 ⁻⁸	4.60 × 10 ⁻⁸	3.70 × 10 ⁻⁸	3.71 × 10 ⁻⁸
46Ti	3.21 × 10 ⁻⁷	9.66 × 10 ⁻⁷	1.57 × 10 ⁻⁶	2.17 × 10 ⁻⁶	4.78 × 10 ⁻⁶	4.95 × 10 ⁻⁶	4.66 × 10 ⁻⁶	5.15 × 10 ⁻⁶	6.32 × 10 ⁻⁶	5.79 × 10 ⁻⁶	5.24 × 10 ⁻⁶	5.96 × 10 ⁻⁶	4.65 × 10 ⁻⁶	4.74 × 10 ⁻⁶
47Ti	1.29 × 10 ⁻⁸	3.38 × 10 ⁻⁸	5.66 × 10 ⁻⁸	7.51 × 10 ⁻⁸	1.50 × 10 ⁻⁷	1.62 × 10 ⁻⁷	1.48 × 10 ⁻⁷	1.69 × 10 ⁻⁷	2.00 × 10 ⁻⁷	1.88 × 10 ⁻⁷	1.71 × 10 ⁻⁷	1.88 × 10 ⁻⁷	1.54 × 10 ⁻⁷	1.54 × 10 ⁻⁷
48Ti	6.11 × 10 ⁻⁶	1.57 × 10 ⁻⁵	3.09 × 10 ⁻⁵	3.83 × 10 ⁻⁵	6.36 × 10 ⁻⁵	7.33 × 10 ⁻⁵	6.93 × 10 ⁻⁵	7.85 × 10 ⁻⁵	8.79 × 10 ⁻⁵	8.60 × 10 ⁻⁵	8.19 × 10 ⁻⁵	8.41 × 10 ⁻⁵	7.41 × 10 ⁻⁵	7.49 × 10 ⁻⁵
49Ti	5.30 × 10 ⁻⁷	1.37 × 10 ⁻⁶	2.68 × 10 ⁻⁶	3.37 × 10 ⁻⁶	5.60 × 10 ⁻⁶	6.70 × 10 ⁻⁶	5.76 × 10 ⁻⁶	7.14 × 10 ⁻⁶	8.07 × 10 ⁻⁶	7.78 × 10 ⁻⁶	7.66 × 10 ⁻⁶	7.48 × 10 ⁻⁶	7.06 × 10 ⁻⁶	6.83 × 10 ⁻⁶
50Ti	2.09 × 10 ⁻⁸	4.41 × 10 ⁻⁸	1.24 × 10 ⁻⁷	1.30 × 10 ⁻⁷	3.30 × 10 ⁻⁷	1.57 × 10 ⁻⁷	5.04 × 10 ⁻⁷	7.14 × 10 ⁻⁷	1.01 × 10 ⁻⁶	1.56 × 10 ⁻⁶	4.38 × 10 ⁻⁶	1.23 × 10 ⁻⁶	3.40 × 10 ⁻⁶	5.28 × 10 ⁻⁶
50V	1.90 × 10 ⁻¹⁰	5.01 × 10 ⁻¹⁰	9.42 × 10 ⁻¹⁰	1.21 × 10 ⁻⁹	2.42 × 10 ⁻⁹	2.53 × 10 ⁻⁹	6.23 × 10 ⁻⁹	2.99 × 10 ⁻⁹	3.00 × 10 ⁻⁹	2.99 × 10 ⁻⁹	2.57 × 10 ⁻⁹	4.22 × 10 ⁻⁹	2.09 × 10 ⁻⁹	2.60 × 10 ⁻⁹
51V	2.89 × 10 ⁻⁶	7.61 × 10 ⁻⁶	1.50 × 10 ⁻⁵	1.92 × 10 ⁻⁵	3.13 × 10 ⁻⁵	3.96 × 10 ⁻⁵	2.79 × 10 ⁻⁵	4.26 × 10 ⁻⁵	9.92 × 10 ⁻⁵	4.58 × 10 ⁻⁵	4.76 × 10 ⁻⁵	4.44 × 10 ⁻⁵	4.65 × 10 ⁻⁵	4.35 × 10 ⁻⁵
50Cr	1.00 × 10 ⁻⁵	3.04 × 10 ⁻⁵	5.40 × 10 ⁻⁵	7.40 × 10 ⁻⁵	1.30 × 10 ⁻⁴	1.61 × 10 ⁻⁴	1.04 × 10 ⁻⁴	1.74 × 10 ⁻⁴	2.02 × 10 ⁻⁴	1.91 × 10 ⁻⁴	2.02 × 10 ⁻⁴	1.87 × 10 ⁻⁴	2.10 × 10 ⁻⁴	1.96 × 10 ⁻⁴
52Cr	2.37 × 10 ⁻⁴	6.06 × 10 ⁻⁴	1.28 × 10 ⁻³	1.58 × 10 ⁻³	2.59 × 10 ⁻³	3.19 × 10 ⁻³	2.45 × 10 ⁻³	3.50 × 10 ⁻³	7.18 × 10 ⁻³	3.73 × 10 ⁻³	3.75 × 10 ⁻³	3.72 × 10 ⁻³	3.54 × 10 ⁻³	3.61 × 10 ⁻³
53Cr	4.43 × 10 ⁻⁵	1.18 × 10 ⁻⁴	2.40 × 10 ⁻⁴	3.08 × 10 ⁻⁴	4.92 × 10 ⁻⁴	6.45 × 10 ⁻⁴	3.95 × 10 ⁻⁴	7.04 × 10 ⁻⁴	1.01 × 10 ⁻³	7.53 × 10 ⁻⁴	8.07 × 10 ⁻⁴	7.15 × 10 ⁻⁴	8.41 × 10 ⁻⁴	8.22 × 10 ⁻⁴
54Cr	7.65 × 10 ⁻⁷	1.68 × 10 ⁻⁶	4.18 × 10 ⁻⁶	4.72 × 10 ⁻⁶	1.04 × 10 ⁻⁵	7.31 × 10 ⁻⁵	7.15 × 10 ⁻⁵	1.07 × 10 ⁻⁴	1.24 × 10 ⁻⁴	8.28 × 10 ⁻⁴	4.65 × 10 ⁻⁴	3.18 × 10 ⁻⁴	2.88 × 10 ⁻⁴	3.75 × 10 ⁻⁴
55Mn	6.89 × 10 ⁻⁴	1.76 × 10 ⁻³	3.67 × 10 ⁻³	4.61 × 10 ⁻³	7.04 × 10 ⁻³	9.47 × 10 ⁻³	5.94 × 10 ⁻³	1.02 × 10 ⁻²	1.13 × 10 ⁻²	1.09 × 10 ⁻²	1.18 × 10 ⁻²	9.90 × 10 ⁻³	1.19 × 10 ⁻²	1.08 × 10 ⁻²
54Fe	4.33 × 10 ⁻³	1.30 × 10 ⁻²	2.50 × 10 ⁻²	3.35 × 10 ⁻²	5.30 × 10 ⁻²	7.36 × 10 ⁻²	3.40 × 10 ⁻²	8.02 × 10 ⁻²	8.38 × 10 ⁻²	8.62 × 10 ⁻²	9.98 × 10 ⁻²	8.03 × 10 ⁻²	1.07 × 10 ⁻¹	9.15 × 10 ⁻²
56Fe	3.53 × 10 ⁻²	7.56 × 10 ⁻²	1.62 × 10 ⁻¹	1.89 × 10 ⁻¹	2.75 × 10 ⁻¹	3.50 × 10 ⁻¹	3.27 × 10 ⁻¹	3.72 × 10 ⁻¹	3.82 × 10 ⁻¹	3.97 × 10 ⁻¹	3.91 × 10 ⁻¹	3.55 × 10 ⁻¹	3.65 × 10 ⁻¹	3.46 × 10 ⁻¹
57Fe	1.30 × 10 ⁻³	2.82 × 10 ⁻³	5.77 × 10 ⁻³	6.88 × 10 ⁻³	9.83 × 10 ⁻³	1.26 × 10 ⁻²	1.03 × 10 ⁻²	1.34 × 10 ⁻²	1.34 × 10 ⁻²	1.43 × 10 ⁻²	1.44 × 10 ⁻²	1.26 × 10 ⁻²	1.38 × 10 ⁻²	1.22 × 10 ⁻²
58Fe	5.69 × 10 ⁻⁶	1.18 × 10 ⁻⁵	3.01 × 10 ⁻⁵	3.32 × 10 ⁻⁵	7.17 × 10 ⁻⁵	5.22 × 10 ⁻⁵	8.57 × 10 ⁻⁵	7.86 × 10 ⁻⁵	5.07 × 10 ⁻⁵	5.98 × 10 ⁻⁵	2.75 × 10 ⁻⁵	2.11 × 10 ⁻⁴	6.80 × 10 ⁻⁴	8.43 × 10 ⁻⁴
59Co	2.82 × 10 ⁻⁵	7.82 × 10 ⁻⁵	1.31 × 10 ⁻⁴	1.84 × 10 ⁻⁴	2.92 × 10 ⁻⁴	3.74 × 10 ⁻⁴	9.01 × 10 ⁻⁴	4.25 × 10 ⁻⁴	7.76 × 10 ⁻⁴	4.65 × 10 ⁻⁴	5.16 × 10 ⁻⁴	4.72 × 10 ⁻⁴	6.07 × 10 ⁻⁴	6.05 × 10 ⁻⁴
58Ni	4.55 × 10 ⁻³	1.16 × 10 ⁻²	2.22 × 10 ⁻²	2.85 × 10 ⁻²	4.20 × 10 ⁻²	5.57 × 10 ⁻²	3.21 × 10 ⁻²	6.01 × 10 ⁻²	5.91 × 10 ⁻²	6.47 × 10 ⁻²	7.09 × 10 ⁻²	5.85 × 10 ⁻²	7.28 × 10 ⁻²	6.03 × 10 ⁻²
60Ni	2.24 × 10 ⁻⁴	6.40 × 10 ⁻⁴	1.10 × 10 ⁻³	1.57 × 10 ⁻³	2.60 × 10 ⁻³	3.33 × 10 ⁻³	4.19 × 10 ⁻³	3.88 × 10 ⁻³	7.55 × 10 ⁻³	4.21 × 10 ⁻³	4.60 × 10 ⁻³	4.42 × 10 ⁻³	5.67 × 10 ⁻³	6.62 × 10 ⁻³
61Ni	3.18 × 10 ⁻⁶	5.36 × 10 ⁻⁶	8.49 × 10 ⁻⁶	9.85 × 10 ⁻⁶	1.39 × 10 ⁻⁵	1.72 × 10 ⁻⁵	1.55 × 10 ⁻⁵	1.93 × 10 ⁻⁵	6.38 × 10 ⁻⁵	2.05 × 10 ⁻⁵	1.64 × 10 ⁻⁵	2.05 × 10 ⁻⁵	1.43 × 10 ⁻⁵	1.54 × 10 ⁻⁵
62Ni	2.71 × 10 ⁻⁵	4.60 × 10 ⁻⁵	7.99 × 10 ⁻⁵	9.07 × 10 ⁻⁵	1.40 × 10 ⁻⁴	1.54 × 10 ⁻⁴	1.28 × 10 ⁻⁴	1.85 × 10 ⁻⁴	2.41 × 10 ⁻⁴	1.82 × 10 ⁻⁴	1.28 × 10 ⁻⁴	2.61 × 10 ⁻⁴	9.59 × 10 ⁻⁴	1.01 × 10 ⁻⁴
64Ni	3.58 × 10 ⁻⁹	6.64 × 10 ⁻⁹	1.82 × 10 ⁻⁸	1.94 × 10 ⁻⁸	4.54 × 10 ⁻⁸	2.32 × 10 ⁻⁸	4.94 × 10 ⁻⁸	3.74 × 10 ⁻⁸	9.48 × 10 ⁻⁸	2.39 × 10 ⁻⁸	5.80 × 10 ⁻⁸	1.60 × 10 ⁻⁷	1.72 × 10 ⁻⁷	2.46 × 10 ⁻⁷
63Cu	2.76 × 10 ⁻⁸	5.24 × 10 ⁻⁸	8.84 × 10 ⁻⁸	1.10 × 10 ⁻⁷	1.67 × 10 ⁻⁷	1.97 × 10 ⁻⁷	9.51 × 10 ⁻⁷	2.32 × 10 ⁻⁷	2.00 × 10 ⁻⁶	2.41 × 10 ⁻⁶	2.05 × 10 ⁻⁶	2.91 × 10 ⁻⁶	1.87 × 10 ⁻⁶	2.21 × 10 ⁻⁶
65Cu	6.57 × 10 ⁻⁹	1.01 × 10 ⁻⁸	1.52 × 10 ⁻⁸	1.64 × 10 ⁻⁸	2.33 × 10 ⁻⁸	3.17 × 10 ⁻⁸	3.61 × 10 ⁻⁸	3.36 × 10 ⁻⁸	3.34 × 10 ⁻⁷	3.60 × 10 ⁻⁷	2.54 × 10 ⁻⁷	3.36 × 10 ⁻⁷	2.38 × 10 ⁻⁷	2.59 × 10 ⁻⁷
64Zn	1.01 × 10 ⁻⁷	1.66 × 10 ⁻⁷	2.45 × 10 ⁻⁷	2.80 × 10 ⁻⁷	3.96 × 10 ⁻⁷	5.53 × 10 ⁻⁷	5.37 × 10 ⁻⁷	5.82 × 10 ⁻⁷	5.95 × 10 ⁻⁷	6.47 × 10 ⁻⁷	5.35 × 10 ⁻⁷	5.16 × 10 ⁻⁷	5.59 × 10 ⁻⁷	6.10 × 10 ⁻⁷
66Zn	1.42 × 10 ⁻⁷	2.18 × 10 ⁻⁷	3.20 × 10 ⁻⁷	3.49 × 10 ⁻⁷	4.74 × 10 ⁻⁷	6.83 × 10 ⁻⁷	8.67 × 10 ⁻⁷	7.10 × 10 ⁻⁷	7.06 × 10 ⁻⁷	7.87 × 10 ⁻⁷	5.84 × 10 ⁻⁷	5.81 × 10 ⁻⁷	5.64 × 10 ⁻⁷	6.10 × 10 ⁻⁷
67Zn	1.00 × 10 ⁻¹⁰	1.50 × 10 ⁻¹⁰	2.18 × 10 ⁻¹⁰	2.37 × 10 ⁻¹⁰	3.18 × 10 ⁻¹⁰	4.60 × 10 ⁻¹⁰	5.59 × 10 ⁻¹⁰	4.73 × 10 ⁻¹⁰	1.10 × 10 ⁻⁹	5.28 × 10 ⁻⁹	3.81 × 10 ⁻⁹	3.91 × 10 ⁻⁹	3.67 × 10 ⁻⁹	3.94 × 10 ⁻⁹
68Zn	6.79 × 10 ⁻¹¹	1.04 × 10 ⁻¹⁰	1.68 × 10 ⁻¹⁰	1.86 × 10 ⁻¹⁰	2.76 × 10 ⁻¹⁰	3.23 × 10 ⁻¹⁰	3.30 × 10 ⁻¹⁰	3.66 × 10 ⁻¹⁰	9.74 × 10 ⁻¹⁰	3.69 × 10 ⁻¹⁰	2.50 × 10 ⁻¹⁰	5.15 × 10 ⁻¹⁰	2.22 × 10 ⁻¹⁰	2.34 × 10 ⁻¹⁰
70Zn	3.06 × 10 ⁻¹⁶	5.32 × 10 ⁻¹⁶	1.39 × 10 ⁻¹⁵	1.46 × 10 ⁻¹⁵	3.46 × 10 ⁻¹⁵	1.29 × 10 ⁻¹⁴	2.71 × 10 ⁻¹⁴	2.12 × 10 ⁻¹⁴	2.11 × 10 ⁻¹⁴	1.15 × 10 ⁻¹⁴	1.69 × 10 ⁻¹⁴	1.37 × 10 ⁻¹⁴	6.93 × 10 ⁻¹⁴	1.17 × 10 ⁻¹⁴
69Ga	3.80 × 10 ⁻¹⁴	7.16 × 10 ⁻¹⁴	1.57 × 10 ⁻¹³	1.75 × 10 ⁻¹³	3.11 × 10 ⁻¹³	2.53 × 10 ⁻¹³	4.89 × 10 ⁻¹³	3.72 × 10 ⁻¹³	9.94 × 10 ⁻¹³	3.09 × 10 ⁻¹³	1.34 × 10 ⁻¹³	7.92 × 10 ⁻¹³	8.76 × 10 ⁻¹³	1.08 × 10 ⁻¹³
71Ga	4.97 × 10 ⁻¹⁶	8.05 × 10 ⁻¹⁶	1.63 × 10 ⁻¹⁵	1.78 × 10 ⁻¹⁵	3.16 × 10 ⁻¹⁵	2.43 × 10 ⁻¹⁵	9.28 × 10 ⁻¹⁵	3.24 × 10 ⁻¹⁵	3.24 × 10 ⁻¹⁵	2.73 × 10 ⁻¹⁵	1.23 × 10 ⁻¹⁵	8.67 × 10 ⁻¹⁵	6.37 × 10 ⁻¹⁵	6.69 × 10 ⁻¹⁵
70Ge	3.10 × 10 ⁻¹⁴	6.53 × 10 ⁻¹⁴	1.25 × 10 ⁻¹³	1.54 × 10 ⁻¹³	2.43 × 10 ⁻¹³	2.51 × 10 ⁻¹³	1.08 × 10 ⁻¹³	3.29 × 10 ⁻¹³	2.78 × 10 ⁻¹³	3.21 × 10 ⁻¹³	2.21 × 10 ⁻¹³	4.94 × 10 ⁻¹³	1.03 × 10 ⁻¹³	1.33 × 10 ⁻¹³

Table B3 – continued

	N1def	N3def	N5def	N10def	N20def	N40def	N100Ldef	N100def	N100Hdef
⁶³ Cu	1.84 × 10 ⁻⁸	1.01 × 10 ⁻⁸	1.28 × 10 ⁻⁸	1.18 × 10 ⁻⁸	3.78 × 10 ⁻⁹	1.28 × 10 ⁻⁹	1.85 × 10 ⁻⁹	3.31 × 10 ⁻¹⁰	2.89 × 10 ⁻⁹
⁶⁵ Cu	8.13 × 10 ⁻⁹	2.12 × 10 ⁻⁹	2.94 × 10 ⁻⁹	2.82 × 10 ⁻⁹	9.83 × 10 ⁻¹⁰	2.15 × 10 ⁻¹⁰	7.57 × 10 ⁻¹⁰	6.17 × 10 ⁻¹¹	3.53 × 10 ⁻¹⁰
⁶⁴ Zn	9.71 × 10 ⁻⁸	3.30 × 10 ⁻⁸	4.57 × 10 ⁻⁸	4.20 × 10 ⁻⁸	1.44 × 10 ⁻⁸	3.00 × 10 ⁻⁹	1.10 × 10 ⁻⁸	9.82 × 10 ⁻¹⁰	1.95 × 10 ⁻¹⁰
⁶⁶ Zn	1.37 × 10 ⁻⁷	4.44 × 10 ⁻⁸	6.36 × 10 ⁻⁸	6.02 × 10 ⁻⁸	2.11 × 10 ⁻⁸	4.32 × 10 ⁻⁹	1.80 × 10 ⁻⁸	1.45 × 10 ⁻⁹	2.45 × 10 ⁻¹⁰
⁶⁷ Zn	1.14 × 10 ⁻¹⁰	3.24 × 10 ⁻¹¹	4.42 × 10 ⁻¹¹	3.97 × 10 ⁻¹¹	1.38 × 10 ⁻¹¹	2.82 × 10 ⁻¹²	1.11 × 10 ⁻¹¹	8.53 × 10 ⁻¹³	1.59 × 10 ⁻¹²
⁶⁸ Zn	5.08 × 10 ⁻¹¹	2.08 × 10 ⁻¹¹	2.96 × 10 ⁻¹¹	2.79 × 10 ⁻¹¹	9.69 × 10 ⁻¹²	2.49 × 10 ⁻¹²	6.63 × 10 ⁻¹²	6.37 × 10 ⁻¹³	1.82 × 10 ⁻¹¹
⁷⁰ Zn	7.57 × 10 ⁻¹⁷	1.12 × 10 ⁻¹⁶	1.70 × 10 ⁻¹⁶	2.31 × 10 ⁻¹⁶	7.43 × 10 ⁻¹⁷	2.04 × 10 ⁻¹⁷	8.31 × 10 ⁻²⁹	4.83 × 10 ⁻¹⁸	5.73 × 10 ⁻¹⁵
⁶⁹ Ga	1.43 × 10 ⁻¹⁴	1.28 × 10 ⁻¹⁴	1.73 × 10 ⁻¹⁴	1.94 × 10 ⁻¹⁴	4.53 × 10 ⁻¹⁵	2.91 × 10 ⁻¹⁵	9.27 × 10 ⁻¹⁷	2.56 × 10 ⁻¹⁶	1.24 × 10 ⁻¹⁴
⁷¹ Ga	2.54 × 10 ⁻¹⁶	1.54 × 10 ⁻¹⁶	2.13 × 10 ⁻¹⁶	2.24 × 10 ⁻¹⁶	6.60 × 10 ⁻¹⁷	2.41 × 10 ⁻¹⁷	1.82 × 10 ⁻¹⁷	3.73 × 10 ⁻¹⁸	6.74 × 10 ⁻¹⁶
⁷⁰ Ge	1.24 × 10 ⁻¹⁴	1.16 × 10 ⁻¹⁴	1.40 × 10 ⁻¹⁴	1.37 × 10 ⁻¹⁴	3.00 × 10 ⁻¹⁵	1.85 × 10 ⁻¹⁵	1.56 × 10 ⁻¹⁸	1.89 × 10 ⁻¹⁶	2.12 × 10 ⁻¹⁵

Table B4. Yields of radioactive isotopes in the bound remnants in solar masses at $t = 100$ s.

	N1def	N3def	N5def	N10def	N20def	N40def	N100Ldef	N100def	N100Hdef
$M_{\text{tot,b}}$	1.32 × 10 ⁺⁰	1.21 × 10 ⁺⁰	1.03 × 10 ⁺⁰	9.26 × 10 ⁻¹	5.45 × 10 ⁻¹	1.90 × 10 ⁻¹	1.33 × 10 ⁻¹	9.0 × 10 ⁻²	1.02 × 10 ⁻¹
¹⁴ C	2.41 × 10 ⁻⁴	1.81 × 10 ⁻⁴	1.22 × 10 ⁻⁴	1.17 × 10 ⁻⁴	8.67 × 10 ⁻⁵	3.55 × 10 ⁻⁵	1.51 × 10 ⁻⁶	1.04 × 10 ⁻⁵	1.72 × 10 ⁻⁵
²² Na	2.33 × 10 ⁻⁷	2.08 × 10 ⁻⁷	1.84 × 10 ⁻⁷	1.77 × 10 ⁻⁷	1.31 × 10 ⁻⁷	6.23 × 10 ⁻⁸	1.16 × 10 ⁻⁹	1.19 × 10 ⁻⁸	8.84 × 10 ⁻⁸
²⁶ Al	3.29 × 10 ⁻⁵	2.86 × 10 ⁻⁵	2.42 × 10 ⁻⁵	2.33 × 10 ⁻⁵	1.77 × 10 ⁻⁵	8.72 × 10 ⁻⁶	1.41 × 10 ⁻⁷	1.44 × 10 ⁻⁶	7.74 × 10 ⁻⁶
³² Si	1.15 × 10 ⁻⁷	1.19 × 10 ⁻⁷	6.92 × 10 ⁻⁸	6.69 × 10 ⁻⁸	4.50 × 10 ⁻⁸	1.70 × 10 ⁻⁸	1.55 × 10 ⁻⁹	3.29 × 10 ⁻⁹	8.68 × 10 ⁻⁹
³² P	5.28 × 10 ⁻⁷	6.33 × 10 ⁻⁷	3.92 × 10 ⁻⁷	4.06 × 10 ⁻⁷	2.38 × 10 ⁻⁷	7.16 × 10 ⁻⁸	1.82 × 10 ⁻⁸	1.73 × 10 ⁻⁸	1.55 × 10 ⁻⁷
³³ P	1.25 × 10 ⁻⁷	1.58 × 10 ⁻⁷	1.06 × 10 ⁻⁷	1.16 × 10 ⁻⁷	5.74 × 10 ⁻⁸	1.57 × 10 ⁻⁸	9.00 × 10 ⁻⁹	5.60 × 10 ⁻⁹	2.65 × 10 ⁻⁸
³³ S	8.80 × 10 ⁻⁸	1.99 × 10 ⁻⁷	1.01 × 10 ⁻⁷	1.34 × 10 ⁻⁷	4.46 × 10 ⁻⁸	4.13 × 10 ⁻⁹	1.45 × 10 ⁻⁸	5.78 × 10 ⁻⁹	1.98 × 10 ⁻⁸
³⁶ Cl	7.35 × 10 ⁻⁸	1.43 × 10 ⁻⁷	8.59 × 10 ⁻⁸	1.13 × 10 ⁻⁷	3.68 × 10 ⁻⁸	3.28 × 10 ⁻⁹	1.30 × 10 ⁻⁸	5.04 × 10 ⁻⁹	8.68 × 10 ⁻⁹
³⁷ Ar	1.20 × 10 ⁻⁶	1.08 × 10 ⁻⁶	1.76 × 10 ⁻⁶	2.23 × 10 ⁻⁶	6.77 × 10 ⁻⁷	6.69 × 10 ⁻⁸	1.91 × 10 ⁻⁷	8.21 × 10 ⁻⁸	7.94 × 10 ⁻⁸
³⁹ Ar	9.22 × 10 ⁻¹⁰	1.63 × 10 ⁻⁹	1.36 × 10 ⁻⁹	2.02 × 10 ⁻⁹	6.97 × 10 ⁻¹⁰	5.07 × 10 ⁻¹¹	1.33 × 10 ⁻¹⁰	5.17 × 10 ⁻¹¹	7.67 × 10 ⁻¹¹
⁴⁰ K	3.60 × 10 ⁻⁹	6.21 × 10 ⁻⁹	5.88 × 10 ⁻⁹	8.75 × 10 ⁻⁹	2.70 × 10 ⁻⁹	1.92 × 10 ⁻¹⁰	5.20 × 10 ⁻¹⁰	2.19 × 10 ⁻¹⁰	2.79 × 10 ⁻¹⁰
⁴¹ Ca	1.90 × 10 ⁻⁷	1.67 × 10 ⁻⁷	2.87 × 10 ⁻⁷	3.62 × 10 ⁻⁷	1.09 × 10 ⁻⁷	1.07 × 10 ⁻⁸	2.80 × 10 ⁻⁸	1.25 × 10 ⁻⁸	1.41 × 10 ⁻⁸
⁴⁴ Ti	2.90 × 10 ⁻⁷	1.44 × 10 ⁻⁷	2.36 × 10 ⁻⁷	2.63 × 10 ⁻⁷	6.67 × 10 ⁻⁸	8.38 × 10 ⁻⁹	3.09 × 10 ⁻⁸	8.97 × 10 ⁻⁹	7.52 × 10 ⁻⁹
⁴⁸ V	5.53 × 10 ⁻⁹	3.74 × 10 ⁻⁹	6.30 × 10 ⁻⁹	9.70 × 10 ⁻⁹	3.11 × 10 ⁻⁹	5.60 × 10 ⁻¹⁰	5.02 × 10 ⁻¹⁰	2.19 × 10 ⁻¹⁰	5.76 × 10 ⁻¹⁰
⁴⁹ V	1.97 × 10 ⁻⁸	1.35 × 10 ⁻⁸	2.19 × 10 ⁻⁸	2.67 × 10 ⁻⁸	7.49 × 10 ⁻⁹	9.90 × 10 ⁻¹⁰	2.66 × 10 ⁻⁹	9.58 × 10 ⁻¹⁰	1.00 × 10 ⁻⁹
⁴⁸ Cr	7.83 × 10 ⁻⁶	4.30 × 10 ⁻⁶	7.21 × 10 ⁻⁶	7.76 × 10 ⁻⁶	1.82 × 10 ⁻⁶	2.37 × 10 ⁻⁷	9.07 × 10 ⁻⁷	2.74 × 10 ⁻⁷	2.21 × 10 ⁻⁷
⁴⁹ Cr	6.19 × 10 ⁻⁷	3.71 × 10 ⁻⁷	5.93 × 10 ⁻⁷	6.58 × 10 ⁻⁷	1.49 × 10 ⁻⁷	2.01 × 10 ⁻⁸	6.96 × 10 ⁻⁸	2.21 × 10 ⁻⁸	2.04 × 10 ⁻⁸
⁵¹ Cr	3.05 × 10 ⁻⁷	2.92 × 10 ⁻⁷	4.13 × 10 ⁻⁷	4.49 × 10 ⁻⁷	1.30 × 10 ⁻⁷	2.10 × 10 ⁻⁸	3.87 × 10 ⁻⁸	1.76 × 10 ⁻⁸	1.62 × 10 ⁻⁸
⁵¹ Mn	2.67 × 10 ⁻⁶	1.70 × 10 ⁻⁶	2.46 × 10 ⁻⁶	2.71 × 10 ⁻⁶	5.69 × 10 ⁻⁷	8.43 × 10 ⁻⁸	2.50 × 10 ⁻⁷	8.98 × 10 ⁻⁸	8.57 × 10 ⁻⁸
⁵² Mn	3.81 × 10 ⁻⁷	2.22 × 10 ⁻⁷	3.34 × 10 ⁻⁷	4.10 × 10 ⁻⁷	1.11 × 10 ⁻⁷	1.86 × 10 ⁻⁸	3.70 × 10 ⁻⁸	1.36 × 10 ⁻⁸	1.93 × 10 ⁻⁸
⁵³ Mn	8.12 × 10 ⁻⁶	8.70 × 10 ⁻⁶	1.06 × 10 ⁻⁵	9.64 × 10 ⁻⁶	2.60 × 10 ⁻⁶	6.73 × 10 ⁻⁷	5.88 × 10 ⁻⁷	3.51 × 10 ⁻⁷	3.99 × 10 ⁻⁷
⁵⁴ Mn	7.35 × 10 ⁻⁸	1.27 × 10 ⁻⁷	1.22 × 10 ⁻⁷	9.59 × 10 ⁻⁸	4.43 × 10 ⁻⁸	1.61 × 10 ⁻⁸	1.23 × 10 ⁻⁹	2.85 × 10 ⁻⁹	1.39 × 10 ⁻⁸
⁵² Fe	2.44 × 10 ⁻⁴	1.42 × 10 ⁻⁴	2.18 × 10 ⁻⁴	2.28 × 10 ⁻⁴	4.80 × 10 ⁻⁵	6.94 × 10 ⁻⁶	2.30 × 10 ⁻⁵	7.84 × 10 ⁻⁶	6.51 × 10 ⁻⁶
⁵³ Fe	3.30 × 10 ⁻⁵	2.09 × 10 ⁻⁵	2.86 × 10 ⁻⁵	3.00 × 10 ⁻⁵	5.72 × 10 ⁻⁶	9.34 × 10 ⁻⁷	2.44 × 10 ⁻⁶	9.73 × 10 ⁻⁷	8.13 × 10 ⁻⁷
⁵⁵ Fe	3.83 × 10 ⁻⁵	6.13 × 10 ⁻⁵	6.96 × 10 ⁻⁵	5.54 × 10 ⁻⁵	1.54 × 10 ⁻⁵	5.03 × 10 ⁻⁶	1.10 × 10 ⁻⁶	1.76 × 10 ⁻⁶	2.05 × 10 ⁻⁶
⁵⁹ Fe	7.60 × 10 ⁻¹¹	1.08 × 10 ⁻¹⁰	1.70 × 10 ⁻¹⁰	1.91 × 10 ⁻¹⁰	6.74 × 10 ⁻¹¹	3.12 × 10 ⁻¹¹	2.75 × 10 ⁻¹⁸	5.45 × 10 ⁻¹²	1.10 × 10 ⁻⁹
⁶⁰ Fe	1.21 × 10 ⁻¹¹	2.03 × 10 ⁻¹¹	3.17 × 10 ⁻¹¹	3.89 × 10 ⁻¹¹	1.42 × 10 ⁻¹¹	5.10 × 10 ⁻¹²	4.71 × 10 ⁻²¹	1.11 × 10 ⁻¹²	6.17 × 10 ⁻¹⁰
⁵⁵ Co	5.36 × 10 ⁻⁴	3.36 × 10 ⁻⁴	4.18 × 10 ⁻⁴	4.24 × 10 ⁻⁴	7.52 × 10 ⁻⁵	1.51 × 10 ⁻⁵	3.11 × 10 ⁻⁵	1.43 × 10 ⁻⁵	9.50 × 10 ⁻⁶
⁵⁶ Co	5.46 × 10 ⁻⁶	4.66 × 10 ⁻⁶	5.27 × 10 ⁻⁶	6.44 × 10 ⁻⁶	2.29 × 10 ⁻⁶	3.94 × 10 ⁻⁷	2.42 × 10 ⁻⁷	1.60 × 10 ⁻⁷	2.48 × 10 ⁻⁷
⁵⁷ Co	1.76 × 10 ⁻⁵	2.88 × 10 ⁻⁵	3.24 × 10 ⁻⁵	2.49 × 10 ⁻⁵	6.81 × 10 ⁻⁶	2.38 × 10 ⁻⁶	2.18 × 10 ⁻⁷	7.47 × 10 ⁻⁷	8.62 × 10 ⁻⁷
⁵⁸ Co	9.90 × 10 ⁻⁸	1.68 × 10 ⁻⁷	1.68 × 10 ⁻⁷	1.21 × 10 ⁻⁷	4.97 × 10 ⁻⁸	1.50 × 10 ⁻⁸	3.22 × 10 ⁻¹⁰	3.54 × 10 ⁻⁹	6.94 × 10 ⁻⁹
⁶⁰ Co	5.65 × 10 ⁻¹⁰	6.93 × 10 ⁻¹⁰	1.00 × 10 ⁻⁹	1.06 × 10 ⁻⁹	3.16 × 10 ⁻¹⁰	2.11 × 10 ⁻¹⁰	1.46 × 10 ⁻¹⁵	2.23 × 10 ⁻¹¹	1.31 × 10 ⁻⁹
⁵⁶ Ni	3.25 × 10 ⁻²	1.59 × 10 ⁻²	2.21 × 10 ⁻²	2.14 × 10 ⁻²	4.45 × 10 ⁻³	7.97 × 10 ⁻⁴	2.62 × 10 ⁻³	7.63 × 10 ⁻⁴	3.79 × 10 ⁻⁴
⁵⁷ Ni	1.05 × 10 ⁻³	5.25 × 10 ⁻⁴	6.79 × 10 ⁻⁴	6.67 × 10 ⁻⁴	1.37 × 10 ⁻⁴	2.76 × 10 ⁻⁵	7.64 × 10 ⁻⁵	2.39 × 10 ⁻⁵	1.08 × 10 ⁻⁵
⁵⁹ Ni	1.12 × 10 ⁻⁵	1.30 × 10 ⁻⁵	1.51 × 10 ⁻⁵	1.24 × 10 ⁻⁵	3.37 × 10 ⁻⁶	1.06 × 10 ⁻⁶	6.37 × 10 ⁻⁷	3.95 × 10 ⁻⁷	3.24 × 10 ⁻⁷
⁶³ Ni	5.10 × 10 ⁻¹⁰	6.30 × 10 ⁻¹⁰	9.60 × 10 ⁻¹⁰	1.05 × 10 ⁻⁹	3.36 × 10 ⁻¹⁰	1.92 × 10 ⁻¹⁰	1.38 × 10 ⁻¹⁷	2.60 × 10 ⁻¹¹	2.45 × 10 ⁻⁹
⁶² Zn	1.54 × 10 ⁻⁵	5.32 × 10 ⁻⁶	8.05 × 10 ⁻⁶	8.48 × 10 ⁻⁶	2.94 × 10 ⁻⁶	5.80 × 10 ⁻⁷	2.53 × 10 ⁻⁶	2.83 × 10 ⁻⁷	3.07 × 10 ⁻⁸
⁶⁵ Zn	3.24 × 10 ⁻¹⁰	8.03 × 10 ⁻¹¹	1.16 × 10 ⁻¹⁰	1.01 × 10 ⁻¹⁰	3.67 × 10 ⁻¹¹	7.95 × 10 ⁻¹²	3.20 × 10 ⁻¹¹	2.35 × 10 ⁻¹²	6.86 × 10 ⁻¹³
⁶⁵ Ga	7.43 × 10 ⁻⁹	1.83 × 10 ⁻⁹	2.57 × 10 ⁻⁹	2.42 × 10 ⁻⁹	8.66 × 10 ⁻¹⁰	1.67 × 10 ⁻¹⁰	7.17 × 10 ⁻¹⁰	5.41 × 10 ⁻¹¹	2.65 × 10 ⁻¹²
⁶⁸ Ge	4.79 × 10 ⁻¹¹	1.74 × 10 ⁻¹¹	2.45 × 10 ⁻¹¹	2.21 × 10 ⁻¹¹	7.88 × 10 ⁻¹²	1.59 × 10 ⁻¹²	6.63 × 10 ⁻¹²	5.06 × 10 ⁻¹³	2.57 × 10 ⁻¹⁴